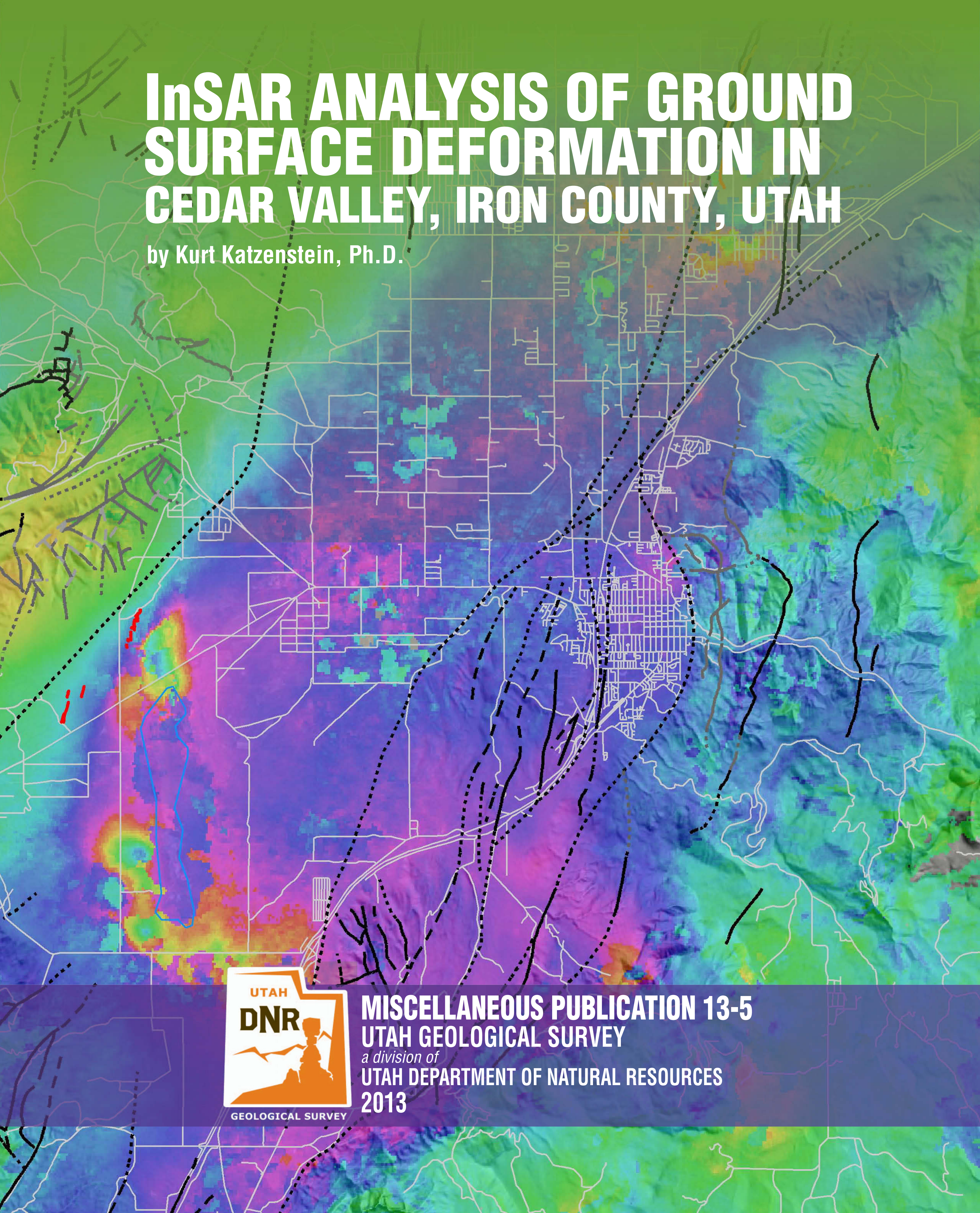

InSAR ANALYSIS OF GROUND SURFACE DEFORMATION IN CEDAR VALLEY, IRON COUNTY, UTAH

by Kurt Katzenstein, Ph.D.

UTAH DNR GEOLOGICAL SURVEY

MISCELLANEOUS PUBLICATION 13-5
UTAH GEOLOGICAL SURVEY
a division of
UTAH DEPARTMENT OF NATURAL RESOURCES
2013

InSAR ANALYSIS OF GROUND SURFACE DEFORMATION IN CEDAR VALLEY, IRON COUNTY, UTAH

by Kurt Katzenstein, Ph.D.
Department of Geology and Geological Engineering
South Dakota School of Mines and Technology

Cover photo: *Semi-cumulative unmasked, composite, stacked unwrapped Envisat interferogram covering the time period of October 26, 2004–August 31, 2010. Each color cycle (fringe) represents 10 cm (3.9 in). This was done to present the result in a manner in which topographic and atmospheric noise is subdued while deformation is dominant. Fault and fissure data from Knudsen and others (2012). All road, DEM, and water-body data downloaded from the USGS National Map (2011).*

ISBN: *978-1-55791-882-6*

MISCELLANEOUS PUBLICATION 13-5
UTAH GEOLOGICAL SURVEY
a division of
UTAH DEPARTMENT OF NATURAL RESOURCES
2013

STATE OF UTAH
Gary R. Herbert, Governor

DEPARTMENT OF NATURAL RESOURCES
Michael Styler, Executive Director

UTAH GEOLOGICAL SURVEY
Richard G. Allis, Director

PUBLICATIONS
contact
Natural Resources Map & Bookstore
1594 W. North Temple
Salt Lake City, UT 84116
telephone: 801-537-3320
toll-free: 1-888-UTAH MAP
website: mapstore.utah.gov
email: geostore@utah.gov

UTAH GEOLOGICAL SURVEY
contact
1594 W. North Temple, Suite 3110
Salt Lake City, UT 84116
telephone: 801-537-3300
website: geology.utah.gov

The Miscellaneous Publication series provides non-UGS authors with a high-quality format for documents concerning Utah geology. Although review comments have been incorporated, this document does not necessarily conform to UGS technical, editorial, or policy standards. The Utah Department of Natural Resources, Utah Geological Survey, makes no warranty, expressed or implied, regarding the suitability of this product for a particular use. The Utah Department of Natural Resources, Utah Geological Survey, shall not be liable under any circumstances for any direct, indirect, special, incidental, or consequential damages with respect to claims by users of this product.

CONTENTS

FIGURES

TABLES

InSAR ANALYSIS OF GROUND SURFACE DEFORMATION IN CEDAR VALLEY, IRON COUNTY, UTAH

by Kurt Katzenstein, Ph.D.

EXECUTIVE SUMMARY

This report documents the results of an Interferometric Synthetic Aperture Radar (InSAR) study that created 24 interferograms covering the 1992–2000 and 2004–2010 time periods. These interferograms revealed several deformation signals in the vicinity of Cedar Valley, Iron County, Utah. The spatial distribution of the deformation signals is consistent with fissuring observed by the Utah Geological Survey in the vicinity of Enoch, Utah, as well as northwest of Quichapa Lake. Deformation is also present in Cedar Valley itself, stretching from the Enoch graben southwest toward Quichapa Lake. In some cases, deformation appears to be controlled by existing structure (faults) and most if not all deformation seems to be coincident with areas of groundwater withdrawal. A stack of five consecutive interferograms from the 1992–2000 time period and a stack of four consecutive interferograms from the 2004–2010 time period are included in this report; however, decorrelation in the vicinity of the Enoch graben makes an estimate of total deformation impossible using the stacks. In total, surface deformation has impacted approximately 256 km^2 (100 mi^2) in Cedar Valley. Subsidence rates in the vicinity of the Enoch graben increased from approximately 0.5–1.0 cm/yr to roughly 1–2 cm/yr after 1999. Near Quichapa Lake, rates appear to have increased from approximately 0–0.5 cm/yr to roughly 2.0–4.0 cm/yr after 1999. Similarly, rates in central Cedar Valley show a general increasing trend after 1999, but rates appear to be more erratic than the other two sites.

BACKGROUND AND PURPOSE

This study originated through discussions with Dr. Steve Bowman, Geologic Hazards Program Manager of the Utah Geological Survey (UGS) in July 2011. Dr. Bowman expressed the UGS's desire to better understand the genesis of multiple fissures that had been observed at two sites in Cedar Valley, Utah, one near Enoch and the other near Quichapa Lake. Not long after these initial discussions, it was established that Interferometric Synthetic Aperture Radar (InSAR) analysis of past and present surface response to groundwater withdrawal could provide insights into the source of the fissuring. Similar studies (such as Amelung and others, 1999, and Buckley, 2000) have confirmed the applicability of this methodology for the goals of this research study. The goal of this research study was to delineate and quantify the present ground surface deformation in Cedar Valley (including the Enoch and Quichapa Lake areas).

APPROACH

The spaceborne Synthetic Aperture Radar (SAR) data utilized for this study were acquired by the European Space Agency's ERS-1, ERS-2, and Envisat satellites from late 1992 through late 2010. Unfortunately, due to a lack of Envisat data coverage for the study area in the early 2000s, there is a four-year time gap between the ERS and Envisat data sets (October 2000 to October 2004).

Radar data were obtained from the Western North America Interferometric Synthetic Aperture Radar Consortium and GeoEarthscope archives operated by UNAVCO, a federally funded clearinghouse for space-platform-based research. As Cedar Valley lies on the boundary between two SAR frames (track 313, frames 2835 and 2853), scenes from independent acquisition dates from each frame were concatenated together such that the entire area of interest could be observed and evaluated. Figure 1 details the areal extent of the two frames. All products shown later in this report are cropped to show the area of interest.

Data were processed using the Repeat Orbit Interferometry Package (ROI_Pac) Version 3.0.1 developed by the NASA Jet Propulsion Laboratory. Scene pairs were selected based on two important parameters:

- Perpendicular Baseline Separation: This represents the perpendicular distance (along satellite track) between the two image acquisitions of interest. Ideally, this value needs to be less than about 250 m (820 ft).
- Date of Acquisition: In general, shorter time periods will have greater coherence (less data dropout). For this study, one-year time periods were studied whenever possible; however, due to lack of data and/or lack of data that satisfy the perpendicular baseline separation requirement, longer time periods were utilized when necessary. Also, the InSAR method does not work well when the ground is covered with snow. Therefore, spring, summer, and fall scenes were utilized for this study.

Two general classes of noise can appear in interferograms created using this processing method: incoherent and coherent noise. Incoherent noise manifests itself as random, speckled (incoherent) pixels, while coherent noise manifests itself as a seemingly coherent signal that is inaccurate. Incoherent noise typically results from:

Figure 1. *Map showing location of the radar images used in this study from Track 313, Frames 2835 and 2853 (upper and lower red boxes respectively). (Source: Base map data from Google Earth and Google maps accessed 11/7/2011.)*

- Snow cover
- Ground disturbance
- Adverse vegetative conditions
- Steep terrain
- Seasonal soil moisture changes (or shallow flooding)

While sources of coherent noise (seemingly coherent signals in the interferogram that do not represent deformation) were minimized whenever possible, some still exist in the data presented in this report. The majority of these types of signals fall into two categories:

- Topographic Signals: As part of the InSAR processing algorithm, the effect of topography is removed from the final product through the use of a reference Digital Elevation Model (DEM). If the DEM contains inaccuracies (commonly resulting from human-caused topography alteration), a coherent erroneous signal will be present in the final product. Furthermore, slight errors in the orbital data (the precise location of the satellite during scene acquisition) can lead to topographic artifacts in the scene as well. This is one of the reasons why smaller perpendicular baselines are preferred. The potential topographic signal that may remain in an interferogram is minimized with a smaller perpendicular baseline difference because the potential parallax is also minimized. Topographic signal can be recognized in an interferogram where a colored fringe pattern exactly corresponds with increasing or decreasing elevation; the rate at which the fringe pattern changes corresponds with the slope of the terrain.
- Atmospheric Signals: While energy from the radar spectrum can easily travel through water vapor, small perturbations in phase can result from SAR arrival-time delays resulting from the energy traveling through a heterogeneous turbulent or stratified (due to extreme topography) atmosphere. This results in a “blotchy” appearance that does not correspond to any real deformation.

Ideally, interferometric pairs using unique scenes can be used to cover roughly the same time period. This allows one to identify which InSAR signals are recurring, and therefore represent actual deformation, and which result from the coherent noise described above.

The initial product of InSAR processing is called a “wrapped interferogram.” A wrapped interferogram is created by subtracting the phase values in each pixel of the “master” image (usually the earlier of the two images of interest) from those contained within the “slave” image.

The result is an image where each pixel represents phase differences varying from 0–2π. These products are often colorized such that one color cycle, or "fringe", represents one full 2π cycle. In the case of C-band radar, such as ERS-1, ERS-2, and Envisat, this corresponds to a 2.83 cm (1.11 in) magnitude of line of sight (LOS) change.

Next, an algorithm is utilized to sum all of the data in the wrapped interferogram so that each pixel contains phase difference in radians. This result is called an unwrapped interferogram and phase change in radians can then be converted to an LOS change in any length unit of interest for a particular study. Another advantage of unwrapped interferograms is that multiple interferograms can be added to one another or "stacked" to evaluate deformation over time periods longer than what is covered by any individual interferogram. All of the results presented in this report are generated from unwrapped interferograms.

Table 1. *List of the interferometric pairs processed for this study. Pairs used for the ERS stack highlighted in green; pairs used for the Envisat stack highlighted in yellow.*

Scene 1 (YYMMDD)	Scene 2 (YYMMDD)	Satellite Platform
921114	930612	ERS
931030	951023	ERS
950919	960521	ERS
950919	970715	ERS
960521	970715	ERS
960521	970819	ERS
970715	991102	ERS
970819	991102	ERS
980421	991102	ERS
980421	001017	ERS
990928	000808	ERS
990928	001017	ERS
991102	001017	ERS
000808	001017	ERS
041026	051115	Envisat
051011	060509	Envisat
051011	060613	Envisat
051115	070911	Envisat
060613	080826	Envisat
070911	080722	Envisat
070911	080826	Envisat
080617	090602	Envisat
080722	090811	Envisat
090811	100831	Envisat

Post-processing of the InSAR results was conducted using the geospatial software ENVI 4.8 and ArcMap 10.0.

Table 1 lists 24 interferograms generated for this study. This list does not include interferograms that failed during processing or successfully processed interferograms of insufficient quality to be included in the report. Once the results were evaluated, the best semi-continuous (covering or nearly covering back-to-back time periods) interferograms for both the ERS (green) and Envisat (yellow) platforms were stacked, or added up to form one interferogram, in order to better quantify surface deformation that occurred during the entire time span covered by each satellite platform. The interferograms chosen for stacking each exhibited the best coherence for the time period covered. The stacks also permitted an estimate of the total areal extent of the deformation that has occurred since 1992. The two stacks are presented here in both raw and masked forms (with an additional stack presented later for the purposes of creating deformation contours). The raw forms include pixels where one or more interferograms contained coherent data. In areas where data were not coherent in all five interferograms, the stack appears "noisier". The masked stacks only contain data in pixels that were coherent in all five interferograms used in the stack. As a result, holes in the data are much larger, but coherent pixels represent accurate quantification of deformation.

GROUNDWATER PUMPING IN CEDAR VALLEY

Most of the water pumped for municipal, agricultural, and domestic use in Cedar Valley, Utah, is withdrawn from alluvial aquifers consisting chiefly of unconsolidated sediments within the valley itself. Producing wells extract as much as 4000 gpm (~6500 acre-ft/yr) (Knudsen and others, 2012). These wells are distributed from within the Enoch graben to southwest of Quichapa Lake as a somewhat continuous zone of production (figure 2). Groundwater production and associated potentiometric surface decline has steadily increased over the time period covered by this study (Knudsen and others, 2012).

Fissuring, thought to be associated with groundwater production, has been observed in the vicinity of the Enoch graben as well as on the northwestern margin of Quichapa Lake. If groundwater pumping is indeed the cause of this fissuring, one would expect the subsidence signal resulting from pumping to mimic the locations of the production wells shown in figure 2.

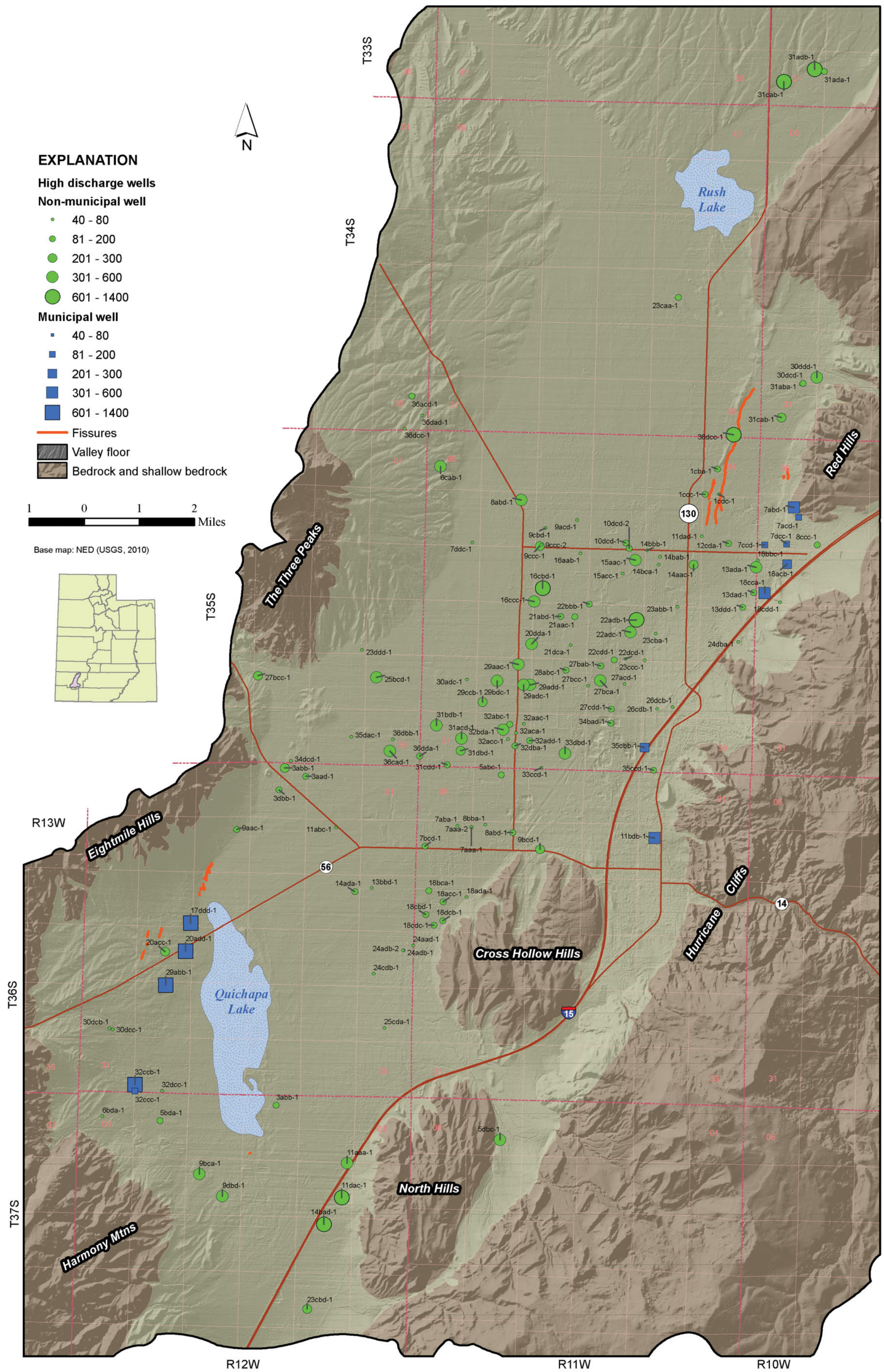

Figure 2. Spatial distribution and magnitude of groundwater production wells in Cedar Valley, Utah. From Knudsen and others (2012).

RESULTS

The results of the InSAR analysis are shown in figures 3–34. The grey pixels show areas of incoherent noise that were masked during the unwrapping process. Figures 17 and 31 represent the cumulative composite stacks constructed from the five most coherent interferograms for the ERS (1992–2000) and Envisat (2004–2010) datasets, respectively. Figures 18 and 32 are similar products where pixels containing no data in any of the interferograms have been masked to ensure data accuracy. Most of the interferograms presented are colorized such that each color cycle (fringe) represents 3 cm (1.2 in) of LOS change. However figures 19, 20, 33, and 34 are colorized at either 6 cm (2.4 in)/fringe (figures 19 and 20), or 10 cm (3.9 in)/fringe (figures 33 and 34). This was done in an effort to suppress atmospheric and topographic noise and enhance deformation.

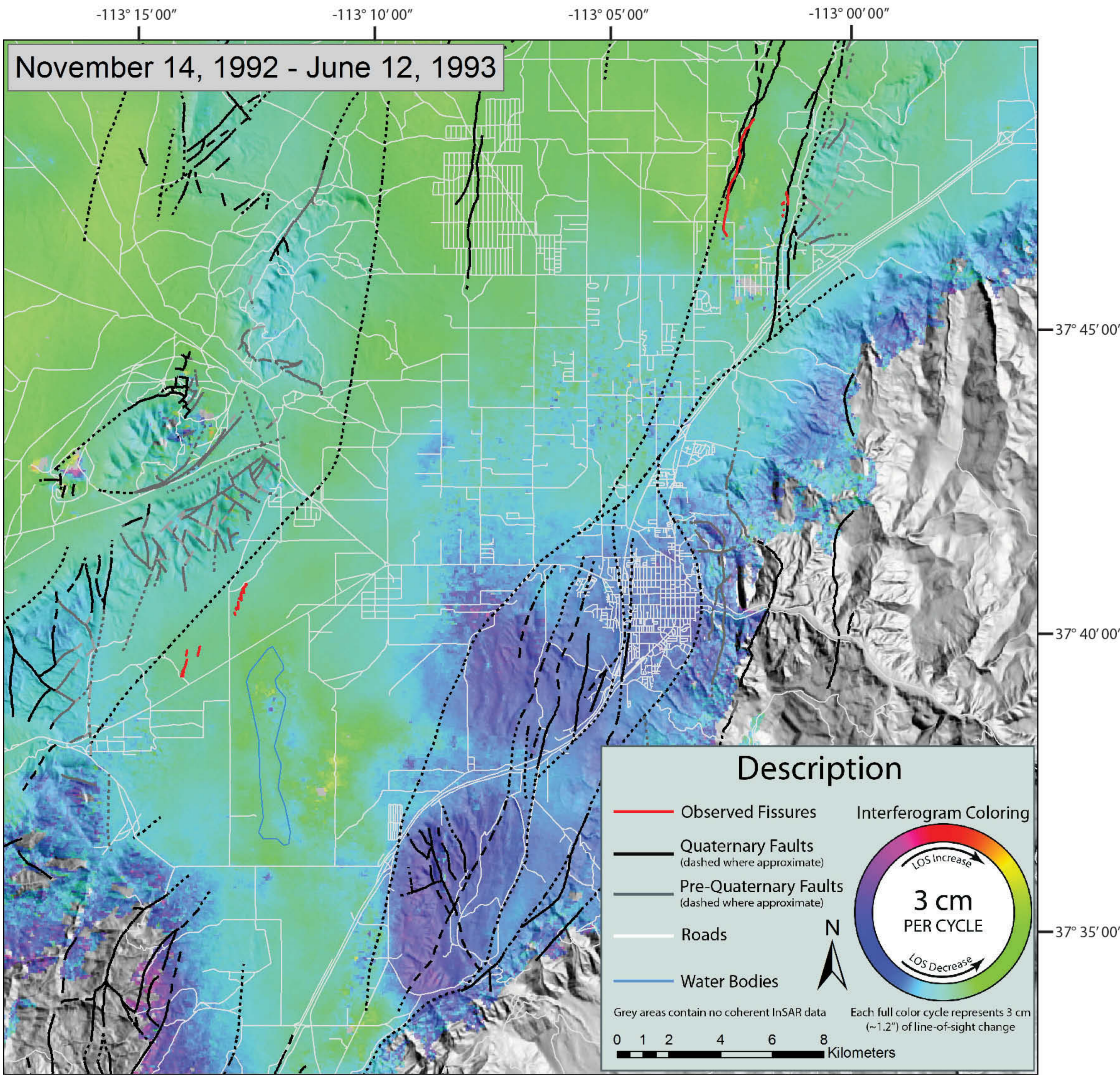

Figure 3. *Unwrapped ERS interferogram covering the time period of November 14, 1992–June 12, 1993. Fault and fissure data from Knudsen and others (2012). All road, DEM, and water-body data downloaded from the USGS National Map (2011).*

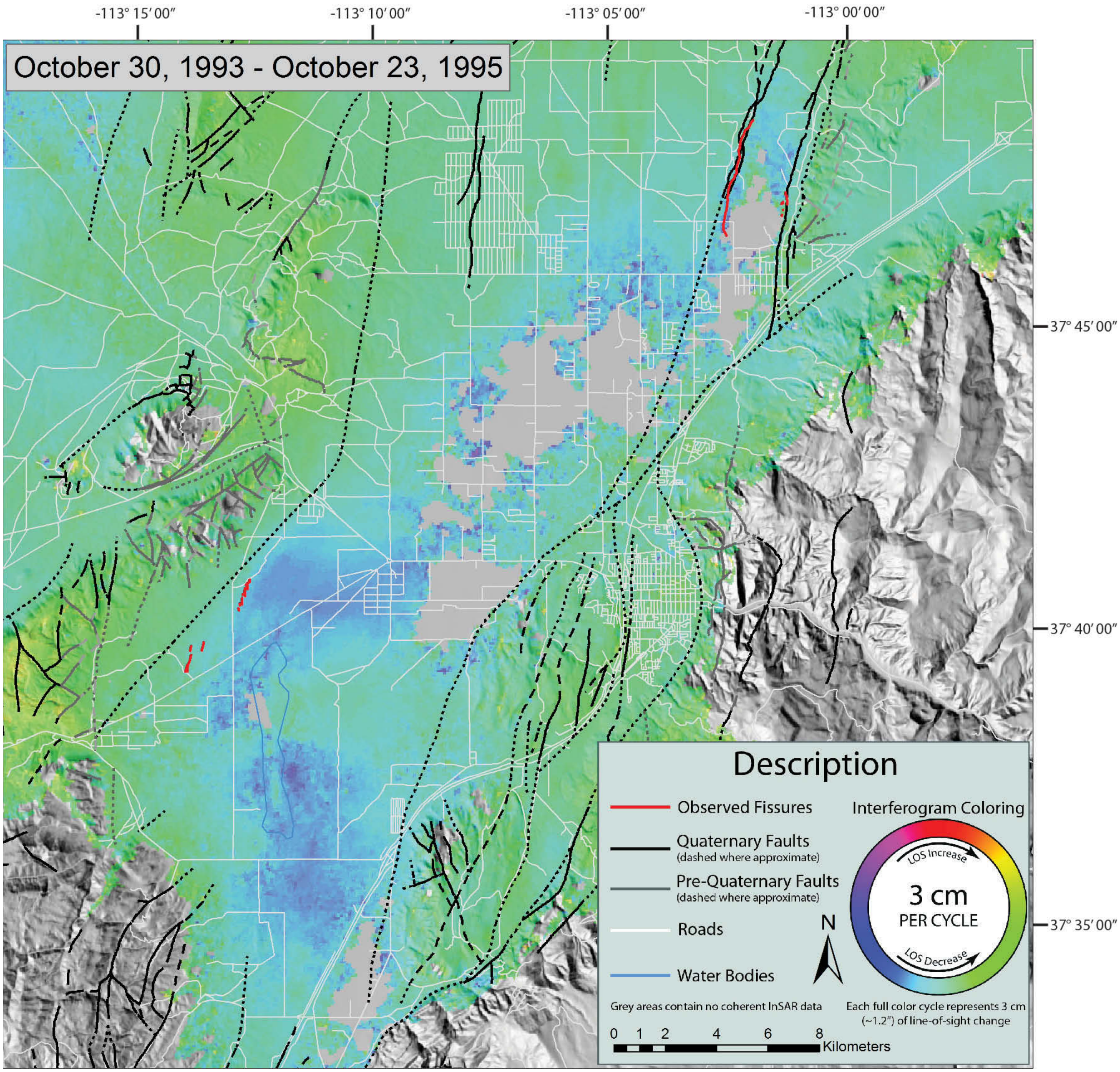

Figure 4. *Unwrapped ERS interferogram covering the time period of October 30, 1993–October 23, 1995. Fault and fissure data from Knudsen and others (2012). All road, DEM, and water-body data downloaded from the USGS National Map (2011).*

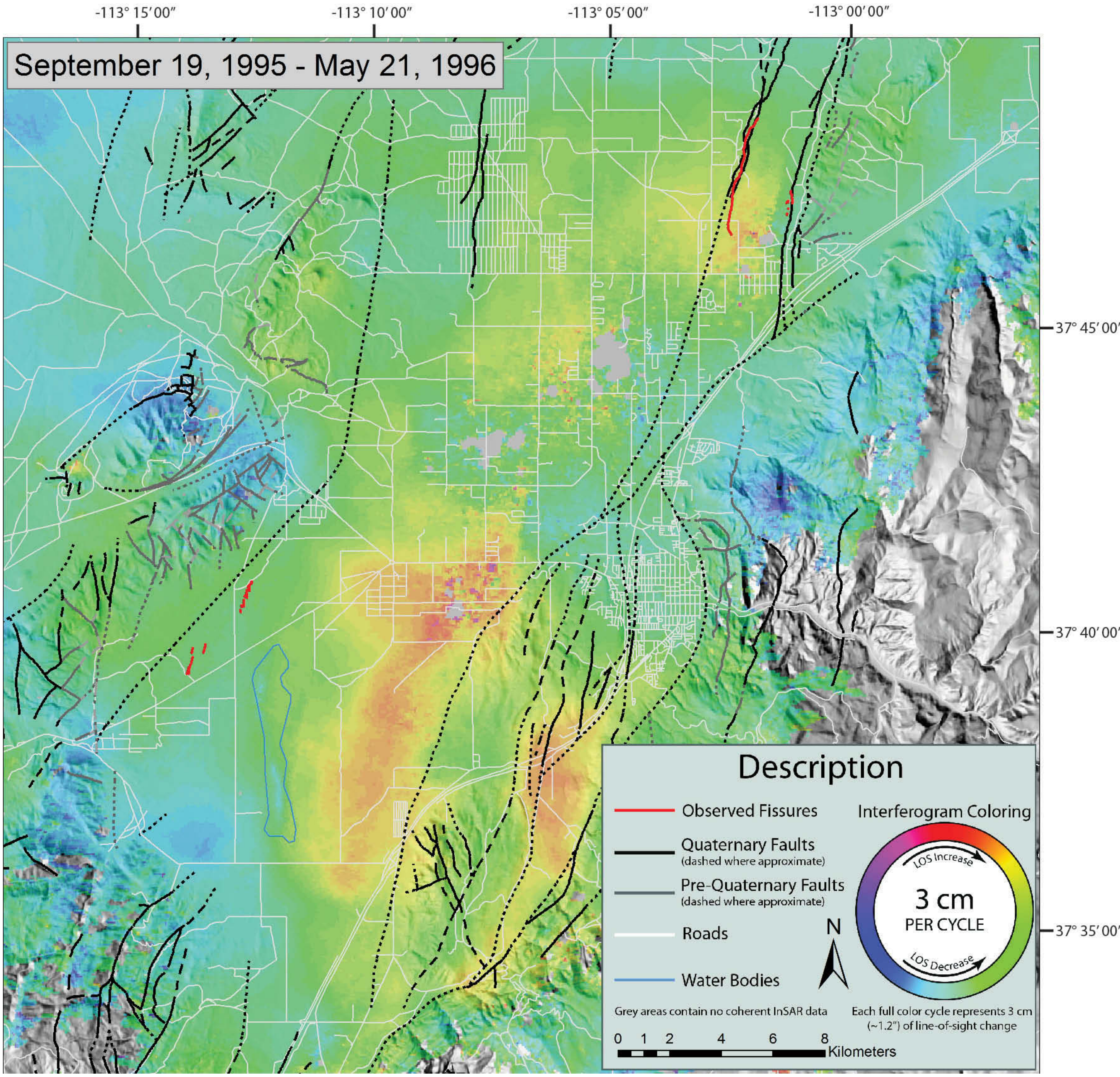

Figure 5. *Unwrapped ERS interferogram covering the time period of September 19, 1995–May 21, 1996. The yellow and orange colors may represent seasonal, elastic recovery of the pumped aquifer. Fault and fissure data from Knudsen and others (2012). All road, DEM, and water-body data downloaded from the USGS National Map (2011).*

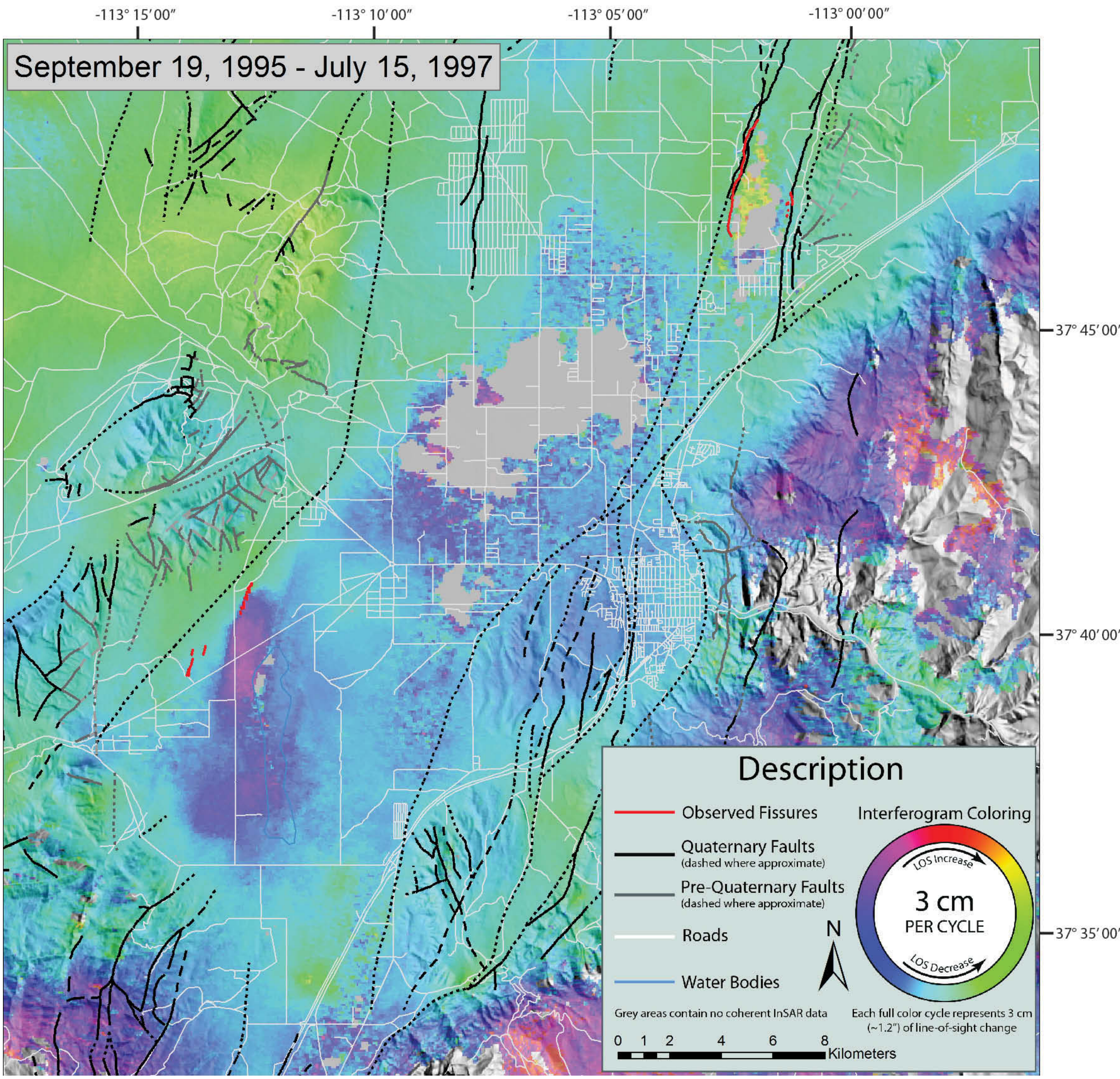

Figure 6. *Unwrapped ERS interferogram covering the time period of September 19, 1995–July 15, 1997. Fault and fissure data from Knudsen and others (2012). All road, DEM, and water-body data downloaded from the USGS National Map (2011).*

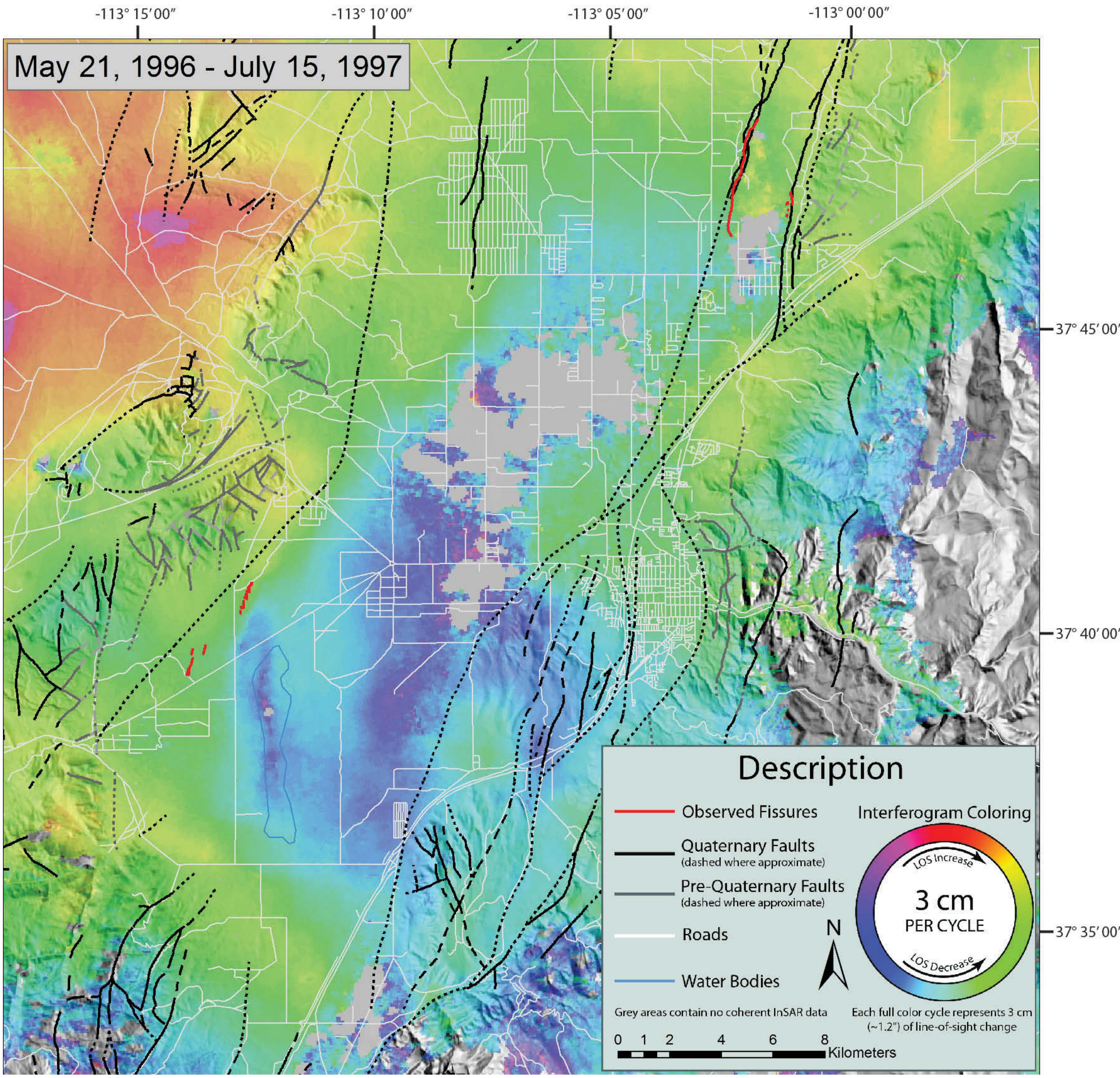

Figure 7. *Unwrapped ERS interferogram covering the time period of May 21, 1996–July 15, 1997. Fault and fissure data from Knudsen and others (2012). All road, DEM, and water-body data downloaded from the USGS National Map (2011).*

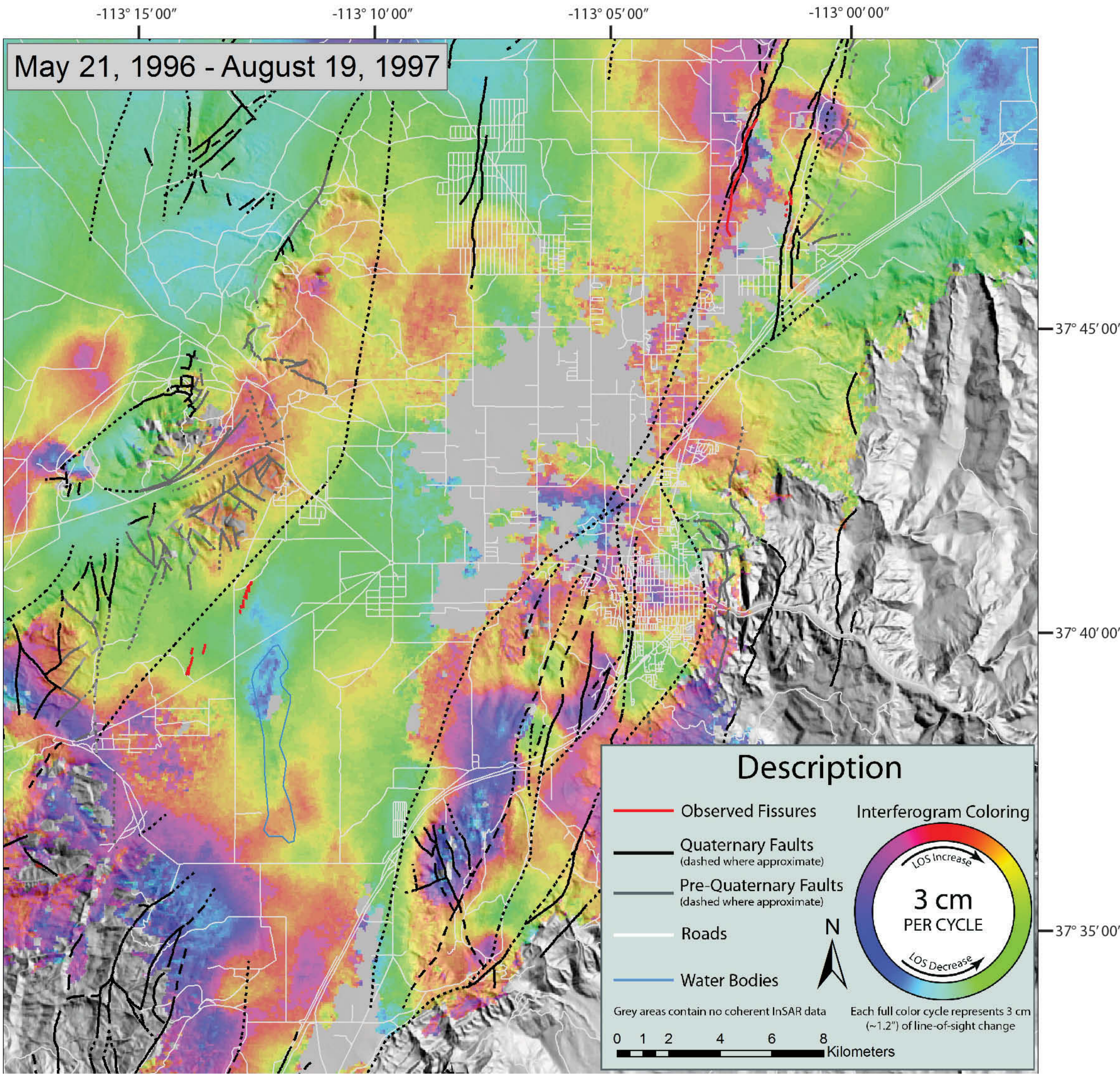

Figure 8. *Unwrapped ERS interferogram covering the time period of May 21, 1996–August 19, 1997. Fault and fissure data from Knudsen and others (2012). All road, DEM, and water-body data downloaded from the USGS National Map (2011).*

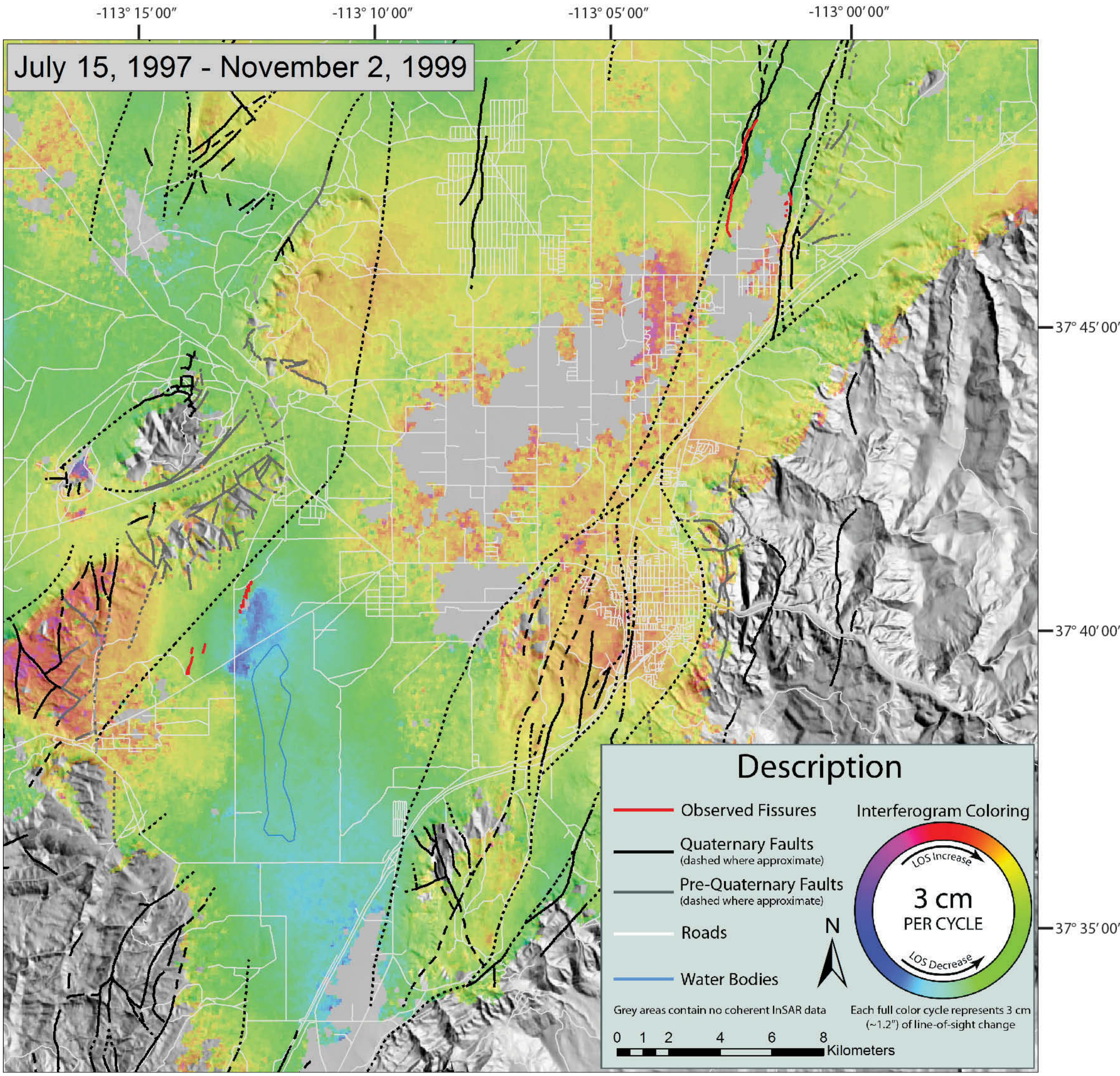

Figure 9. *Unwrapped ERS interferogram covering the time period of July 15, 1997–November 2, 1999. Fault and fissure data from Knudsen and others (2012). All road, DEM, and water-body data downloaded from the USGS National Map (2011).*

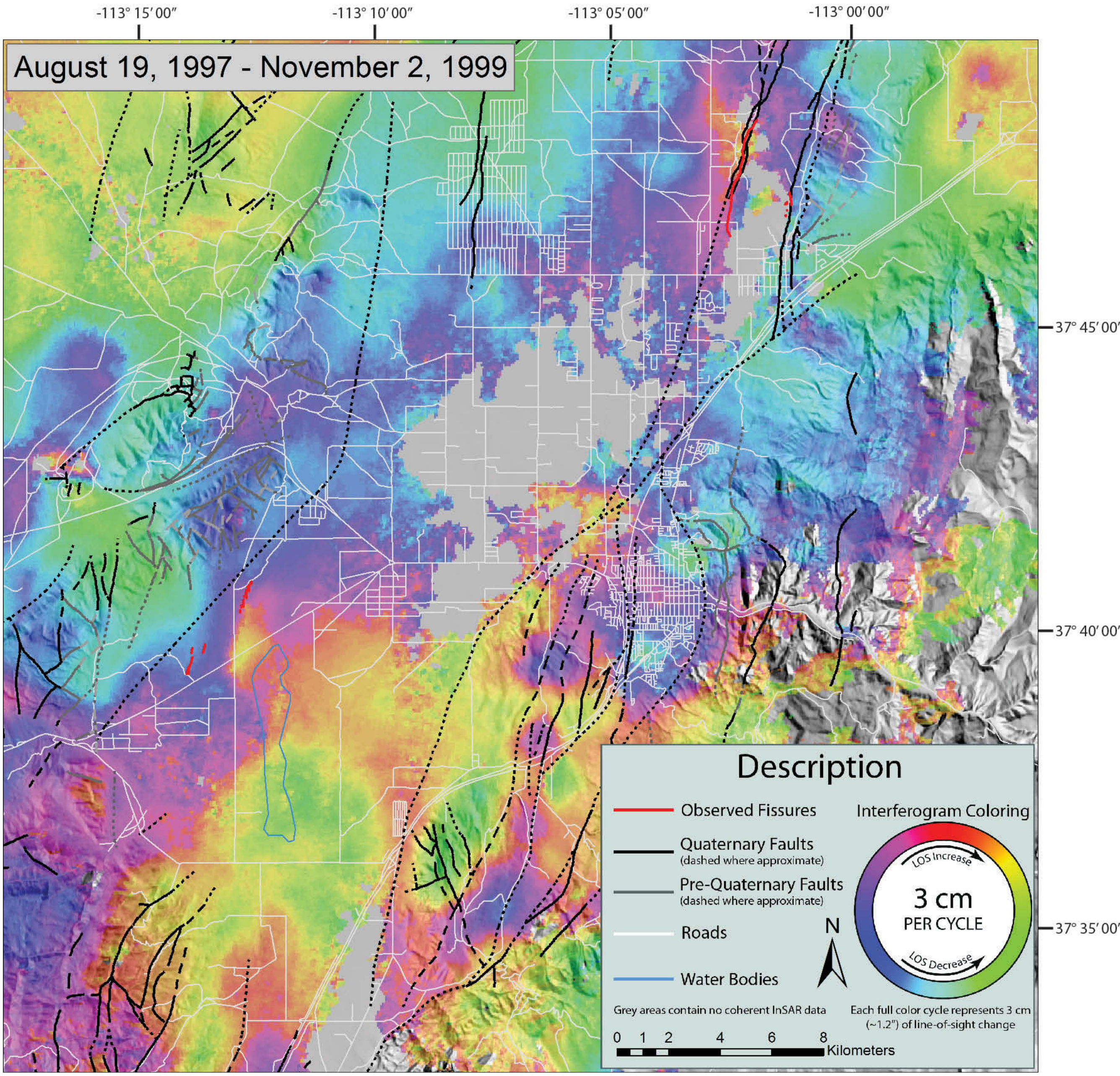

Figure 10. *Unwrapped ERS interferogram covering the time period of August 19, 1997–November 2, 1999. Fault and fissure data from Knudsen and others (2012). All road, DEM, and water-body data downloaded from the USGS National Map (2011).*

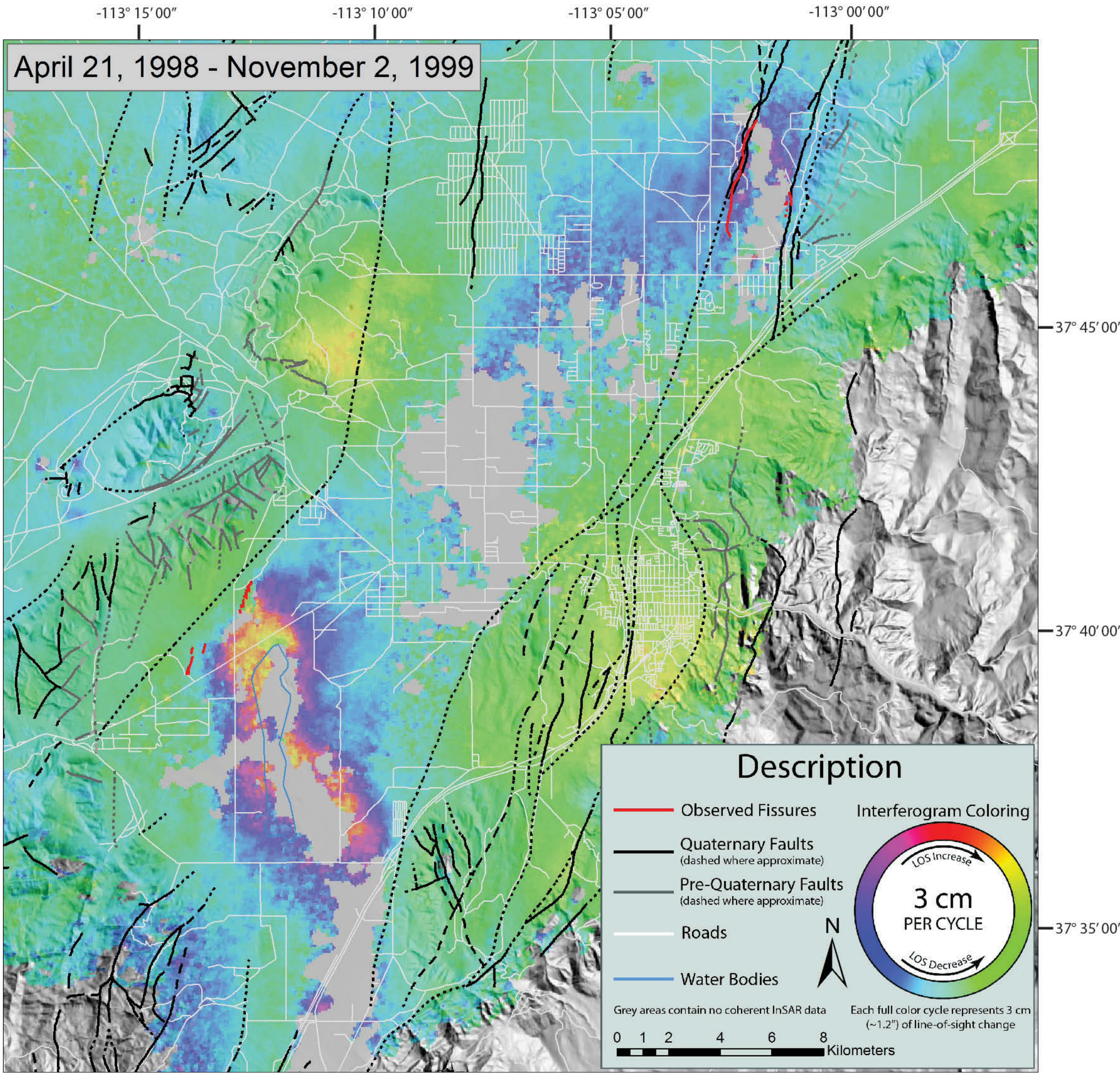

Figure 11. *Unwrapped ERS interferogram covering the time period of April 21, 1998 - November 2, 1999. Fault and fissure data from Knudsen and others (2012). All road, DEM, and water-body data downloaded from the USGS National Map (2011).*

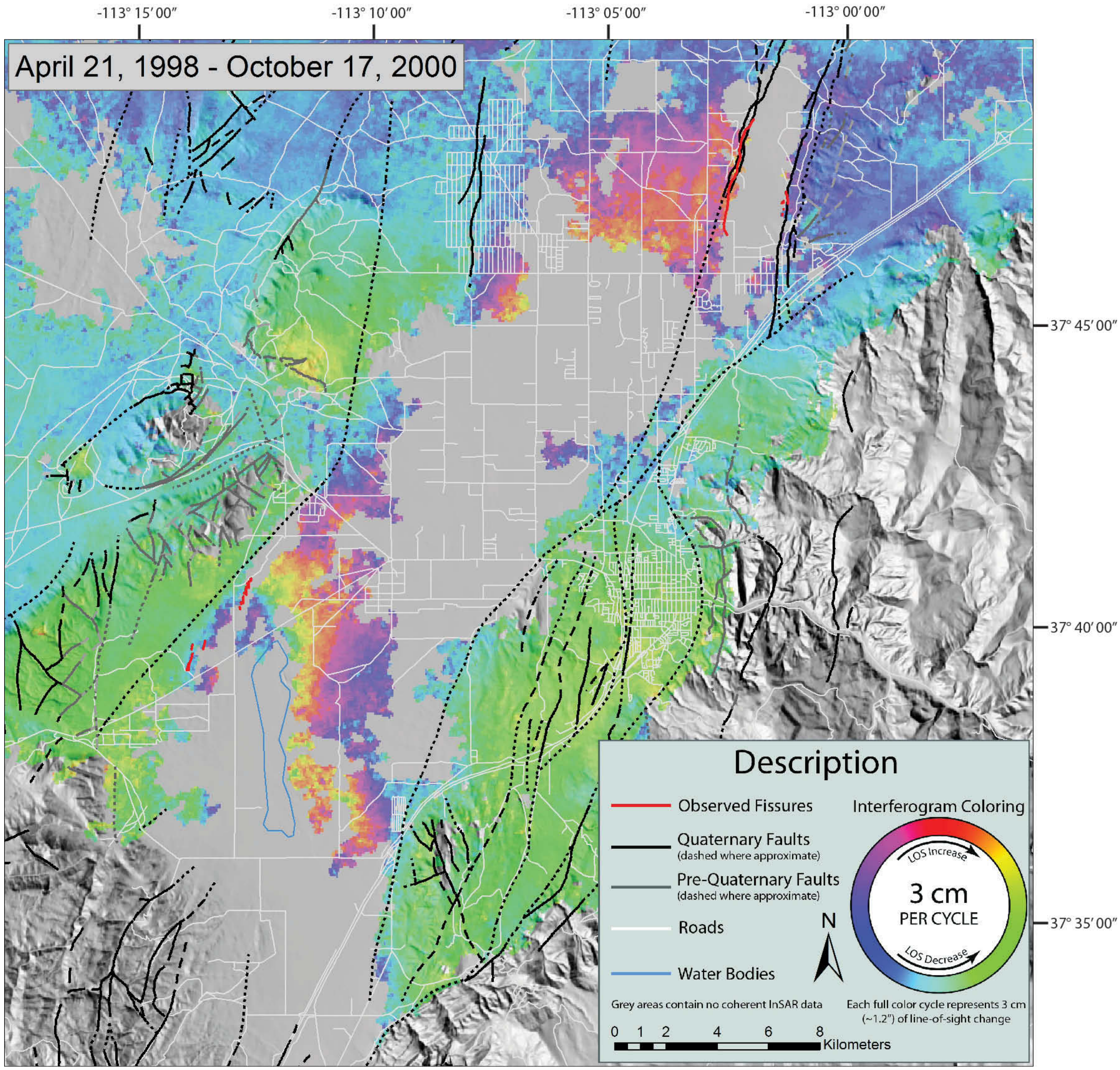

Figure 12. *Unwrapped ERS interferogram covering the time period of April 21, 1998–October 17, 2000. Fault and fissure data from Knudsen and others (2012). All road, DEM, and water-body data downloaded from the USGS National Map (2011).*

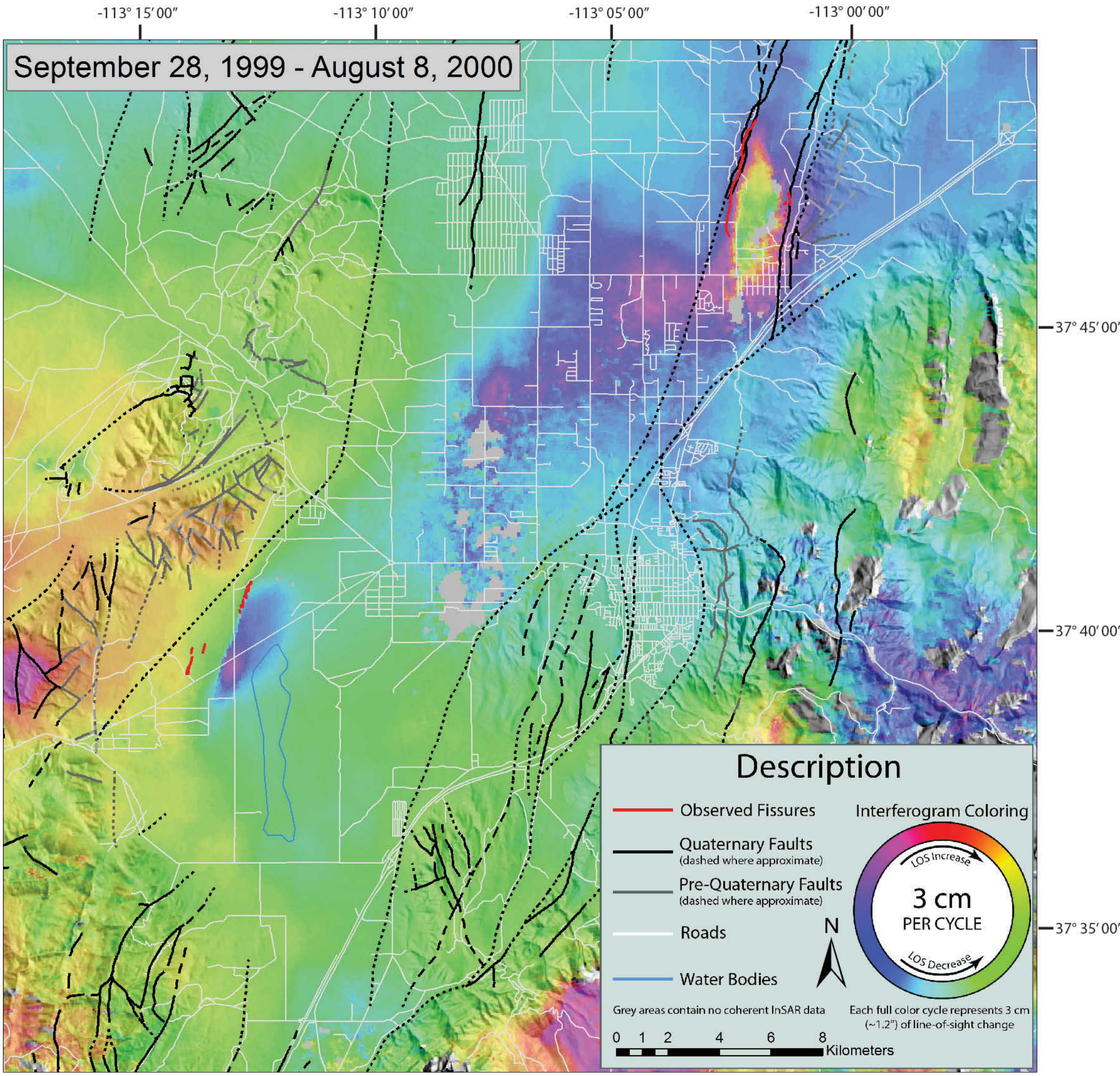

Figure 13. *Unwrapped ERS interferogram covering the time period of September 28, 1999–August 8, 2000. Fault and fissure data from Knudsen and others (2012). All road, DEM, and water-body data downloaded from the USGS National Map (2011).*

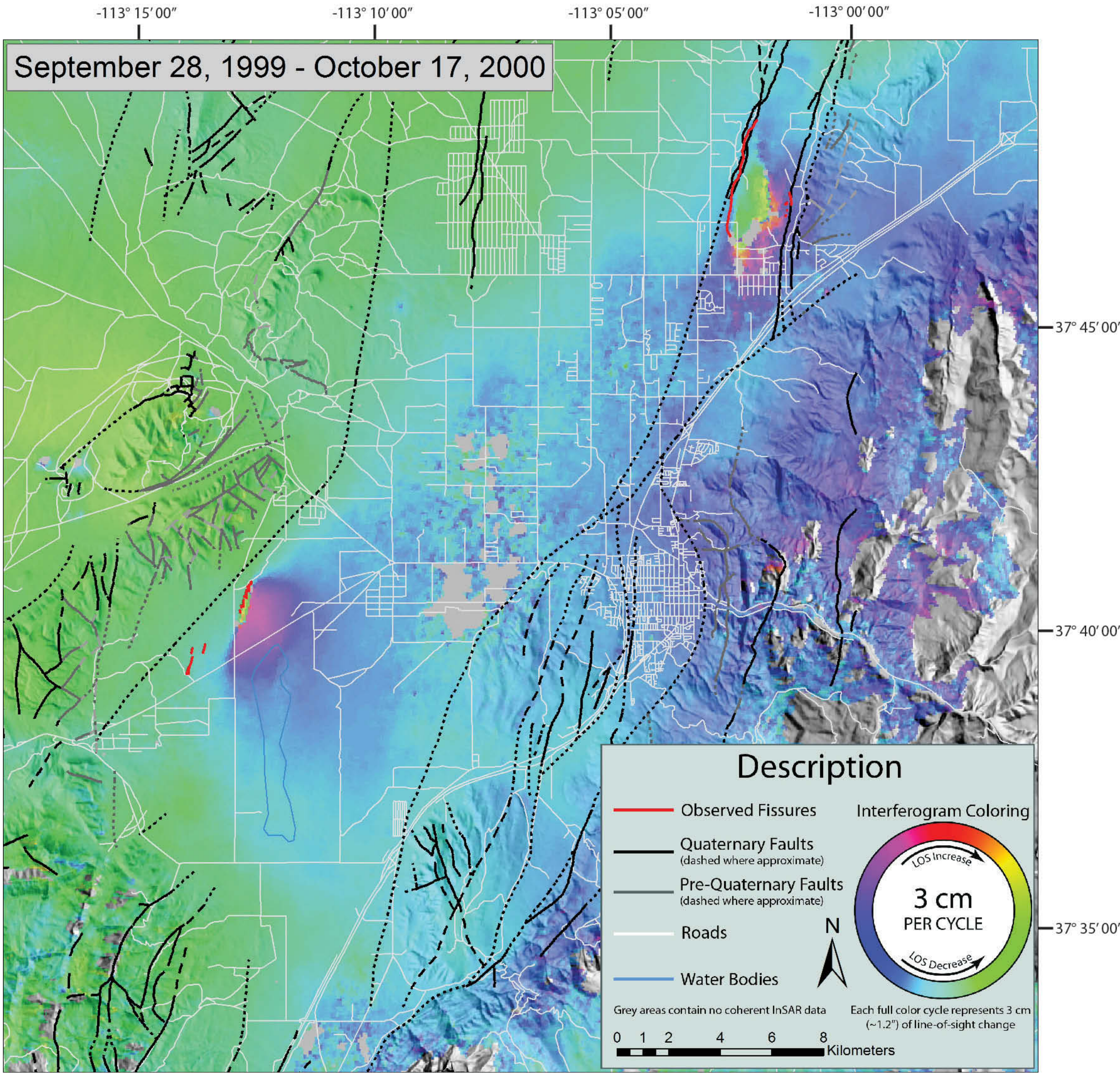

Figure 14. *Unwrapped ERS interferogram covering the time period of September 28, 1999–October 17, 2000. Fault and fissure data from Knudsen and others (2012). All road, DEM, and water-body data downloaded from the USGS National Map (2011).*

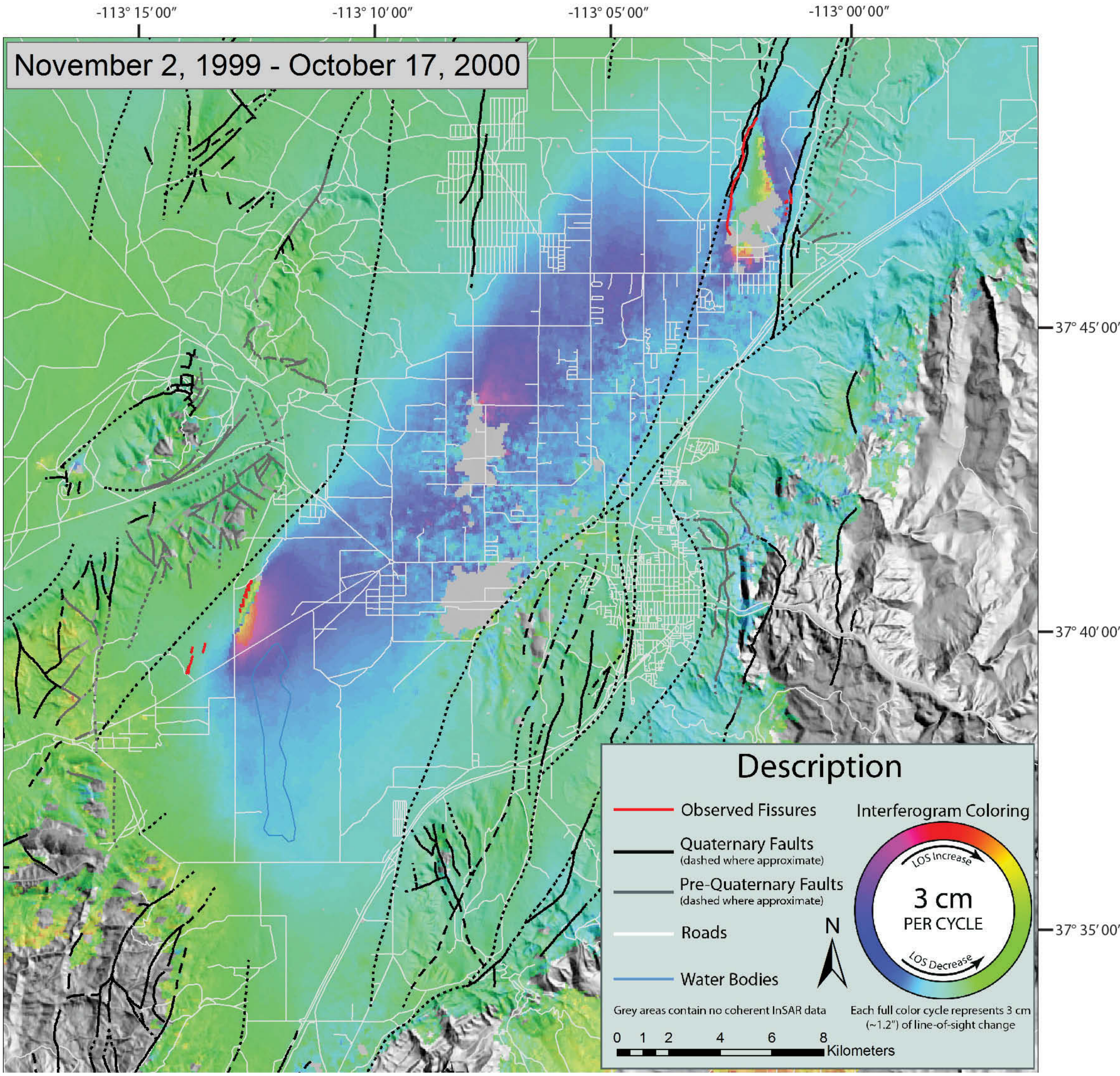

Figure 15. *Unwrapped ERS interferogram covering the time period of November 2, 1999–October 17, 2000. Fault and fissure data from Knudsen and others (2012). All road, DEM, and water-body data downloaded from the USGS National Map (2011).*

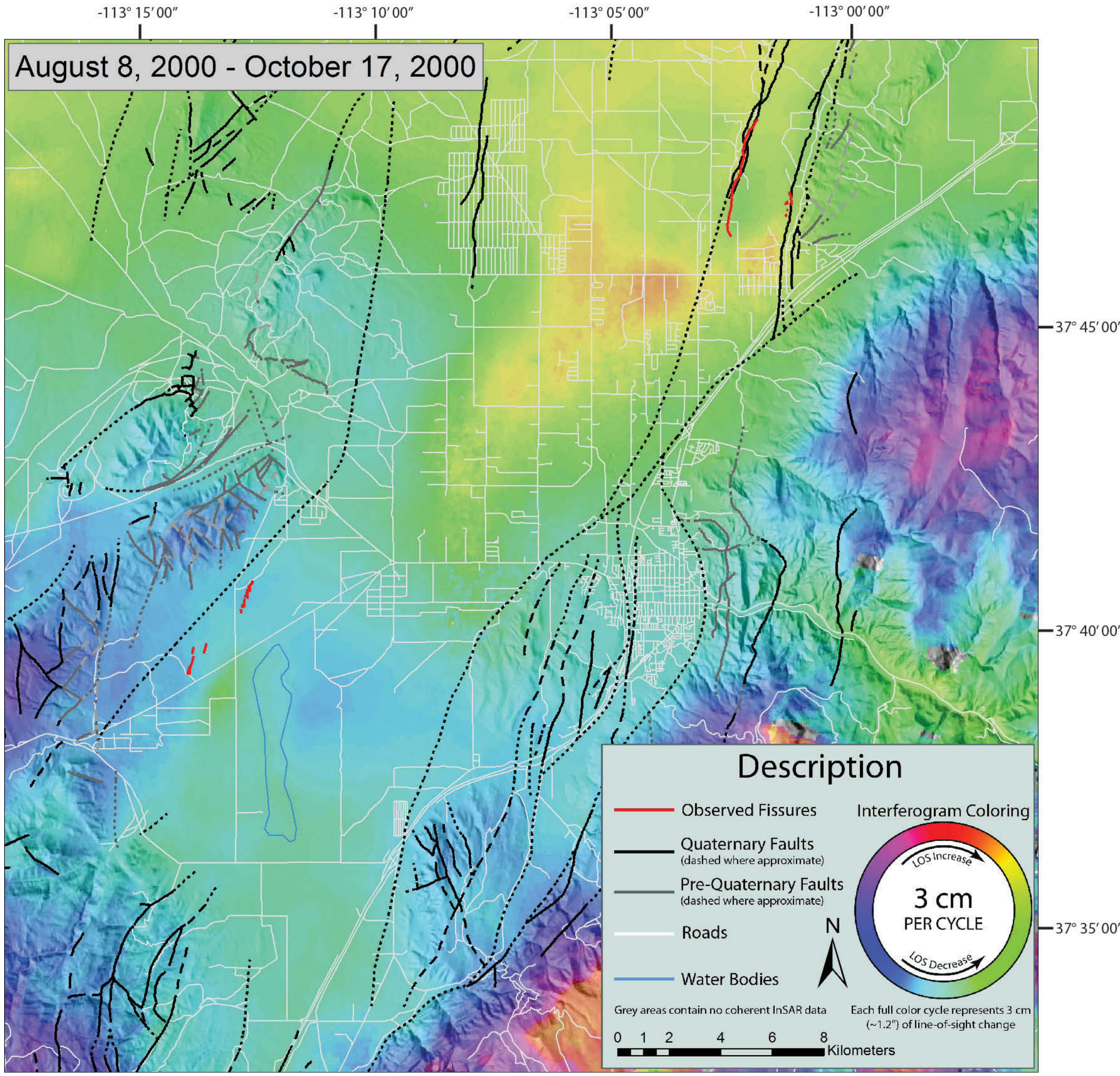

Figure 16. *Unwrapped ERS interferogram covering the time period of August 8, 2000–October 17, 2000. Fault and fissure data from Knudsen and others (2012). All road, DEM, and water-body data downloaded from the USGS National Map (2011).*

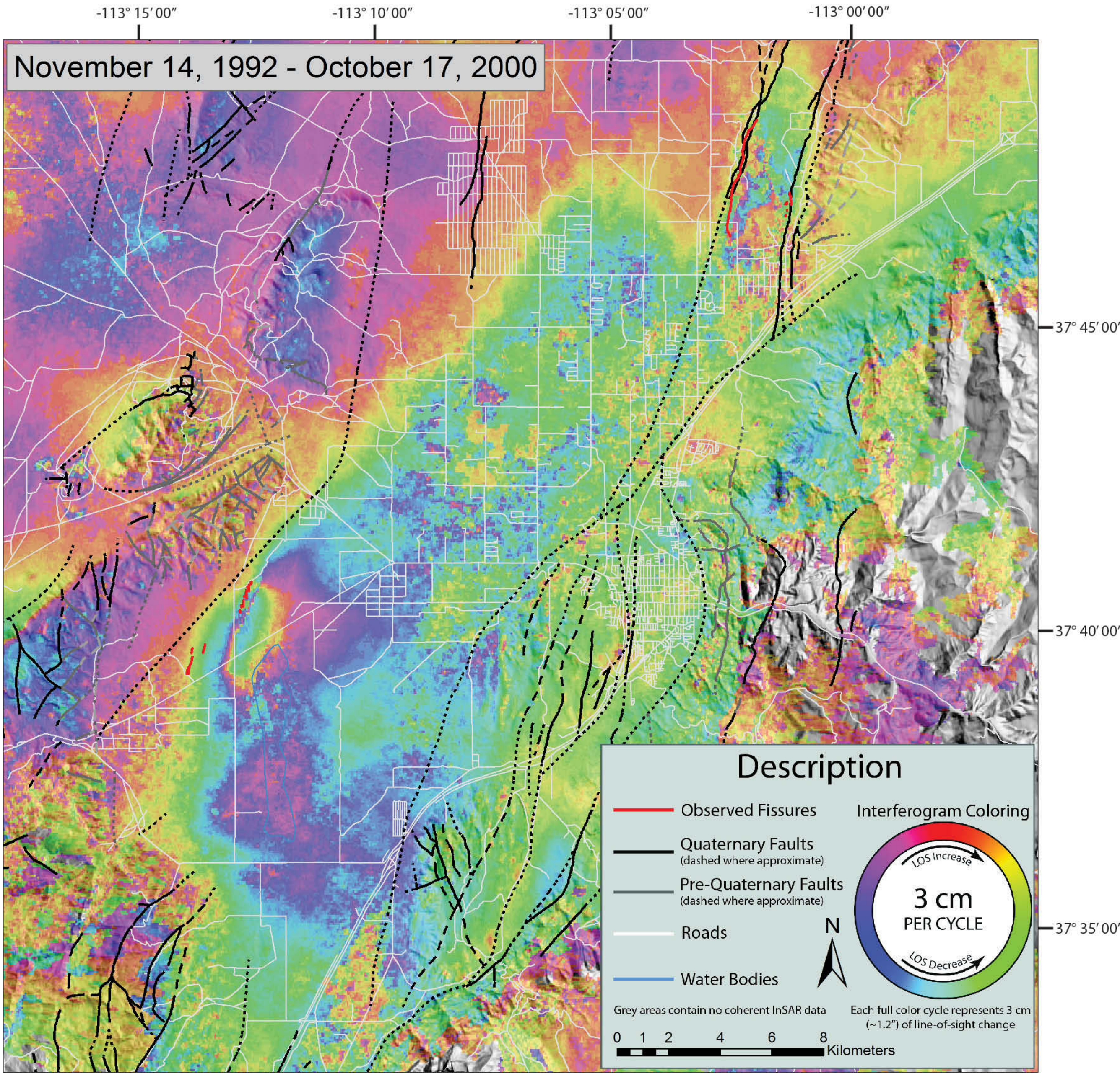

Figure 17. *Semi-cumulative composite, stacked unwrapped ERS interferogram covering the time period November 14, 1992–October 17, 2000. Note that some pixels were not coherent in all five interferograms used to create the stack; this can lead to a noisy or "speckeled" look. See figure 18 for a masked version of this stack where each pixel with data represents deformation that was coherent in every interferogram used to create the stack. Fault and fissure data from Knudsen and others (2012). All road, DEM, and water-body data downloaded from the USGS National Map (2011).*

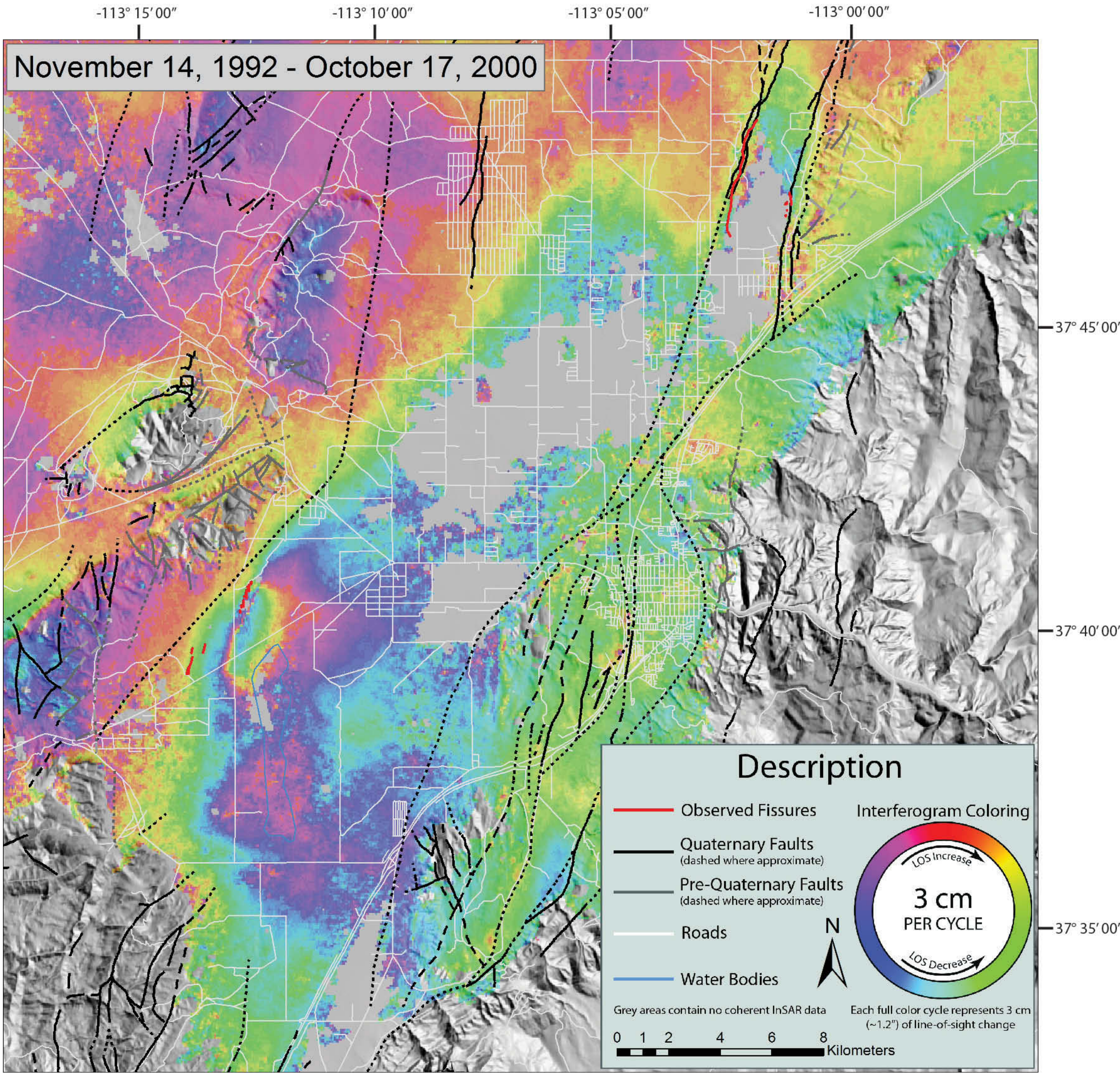

Figure 18. *Semi-cumulative masked, composite, stacked unwrapped ERS interferogram covering the time period of November 14, 1992–October 17, 2000. This stack is masked such that each pixel with data represents deformation that was coherent in every interferogram used to create the stack. Fault and fissure data from Knudsen and others (2012). All road, DEM, and water-body data downloaded from the USGS National Map (2011).*

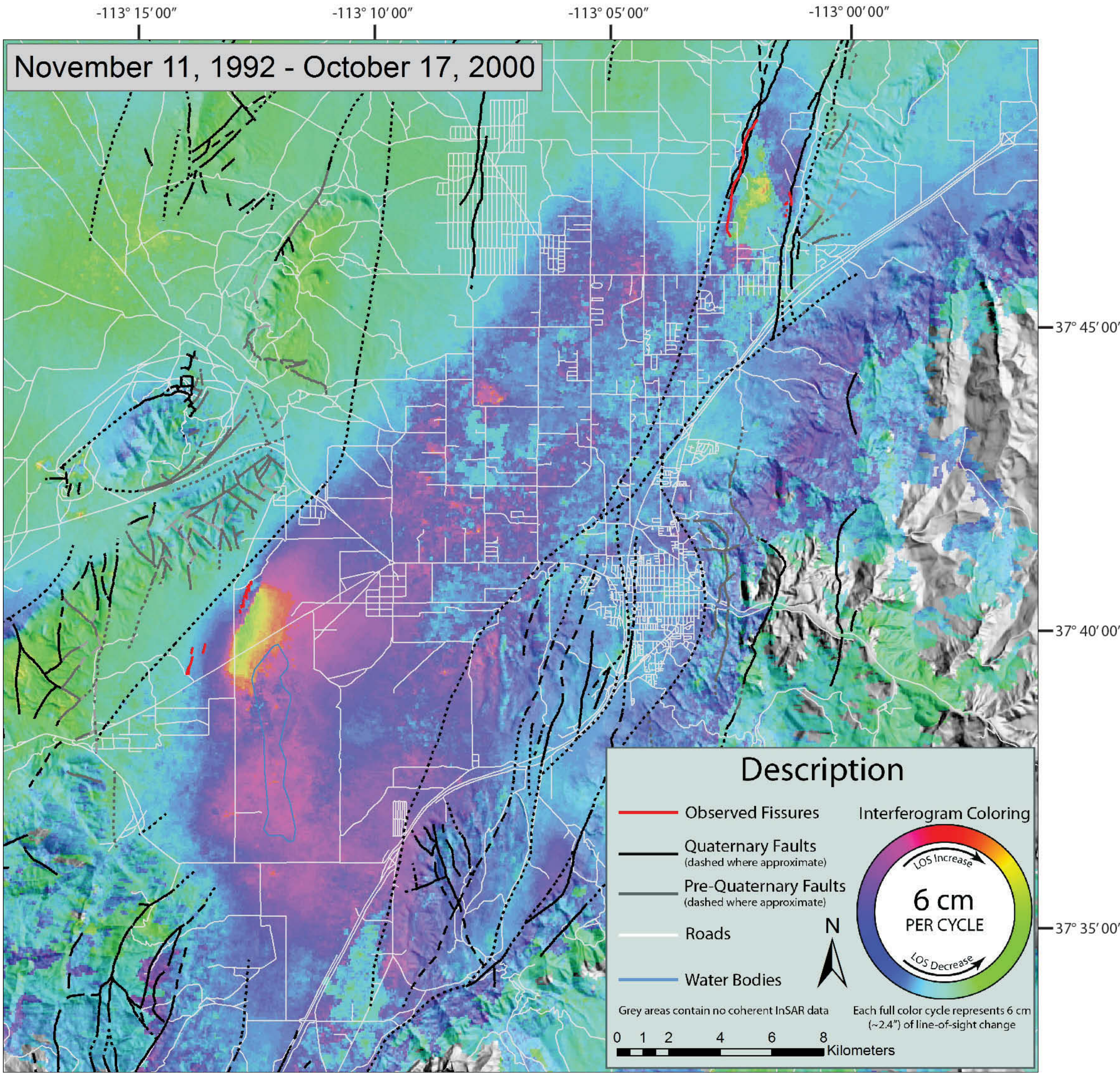

Figure 19. *Semi-cumulative unmasked, composite, stacked unwrapped ERS interferogram covering the time period of November 14, 1992–October 17, 2000. This stack is identical to the one presented in figure 17 except each color cycle (fringe) represents 6 cm (2.4 in). This was done to present the result in a manner in which topographic and atmospheric noise is subdued while deformation is dominant. Fault and fissure data from Knudsen and others (2012). All road, DEM, and water-body data downloaded from the USGS National Map (2011).*

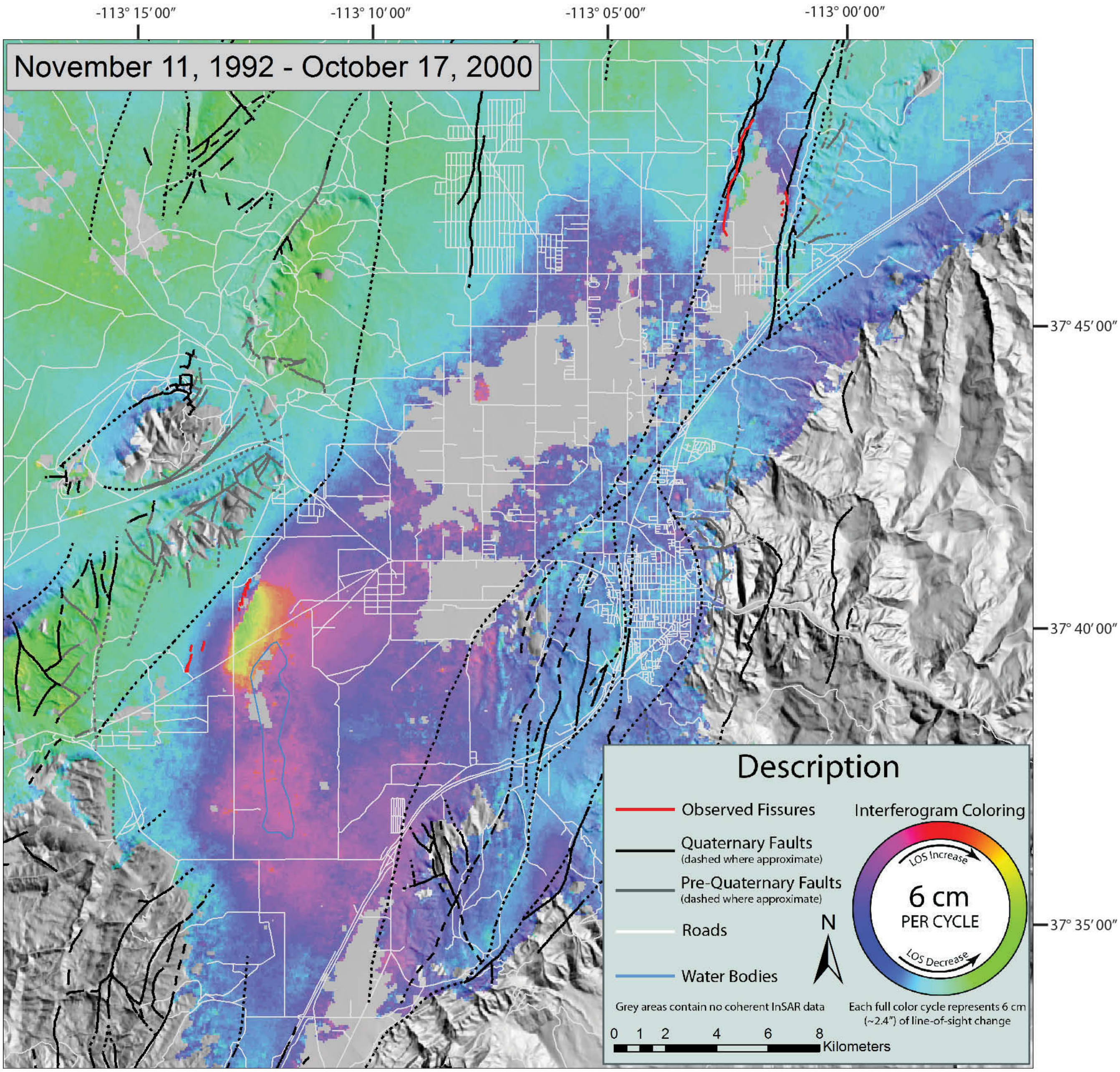

Figure 20. *Semi-cumulative masked, composite, stacked unwrapped ERS interferogram covering the time period of November 14, 1992–October 17, 2000. This stack is identical to the one presented in figure 18 except each color cycle (fringe) represents 6 cm (2.4 in). This was done to present the result in a manner in which topographic and atmospheric noise is subdued while deformation is dominant. Fault and fissure data from Knudsen and others (2012). All road, DEM, and water-body data downloaded from the USGS National Map (2011).*

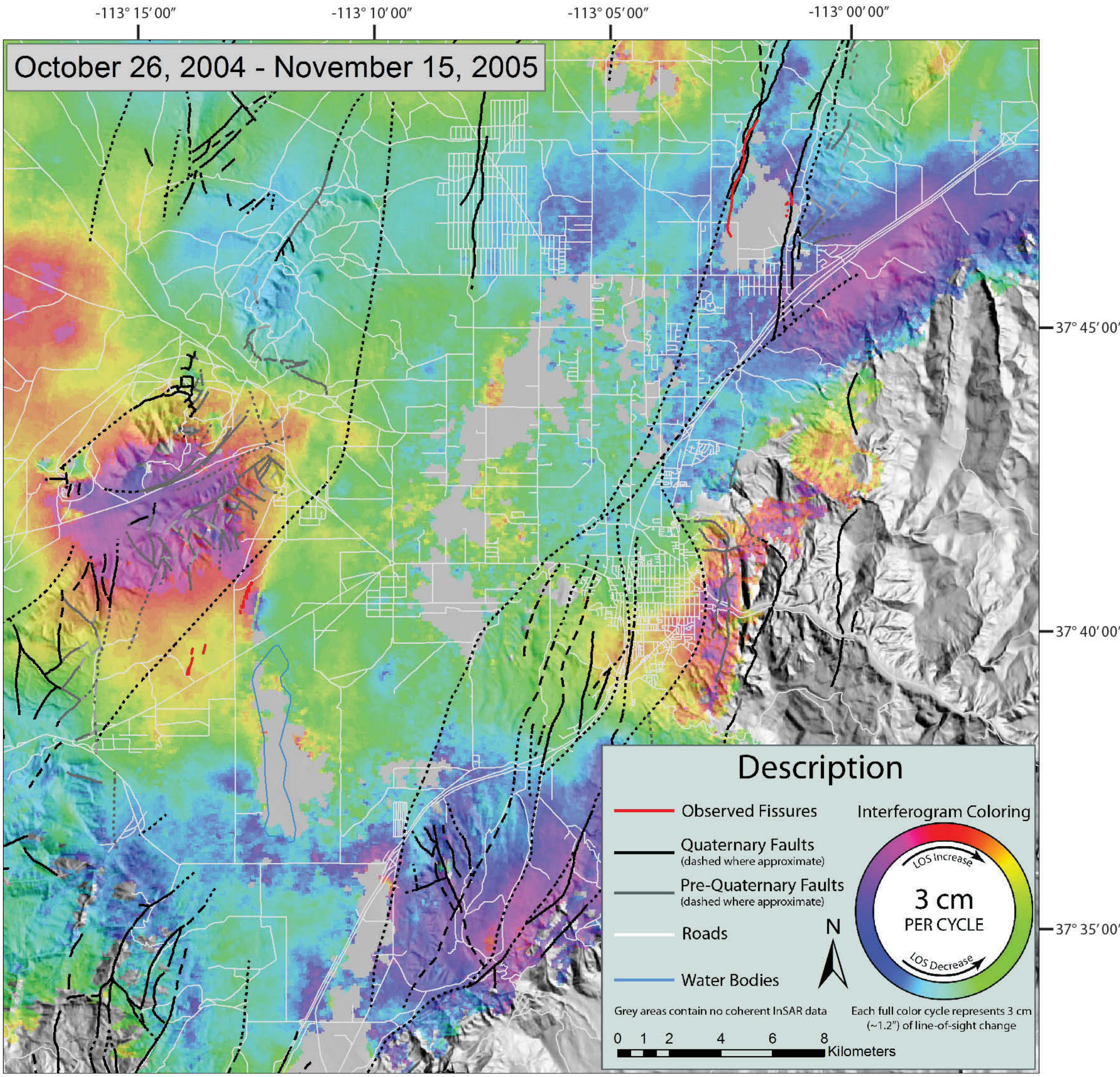

Figure 21. *Unwrapped Envisat interferogram covering the time period of October 26, 2004–November 15, 2005. Fault and fissure data from Knudsen and others (2012). All road, DEM, and water-body data downloaded from the USGS National Map (2011).*

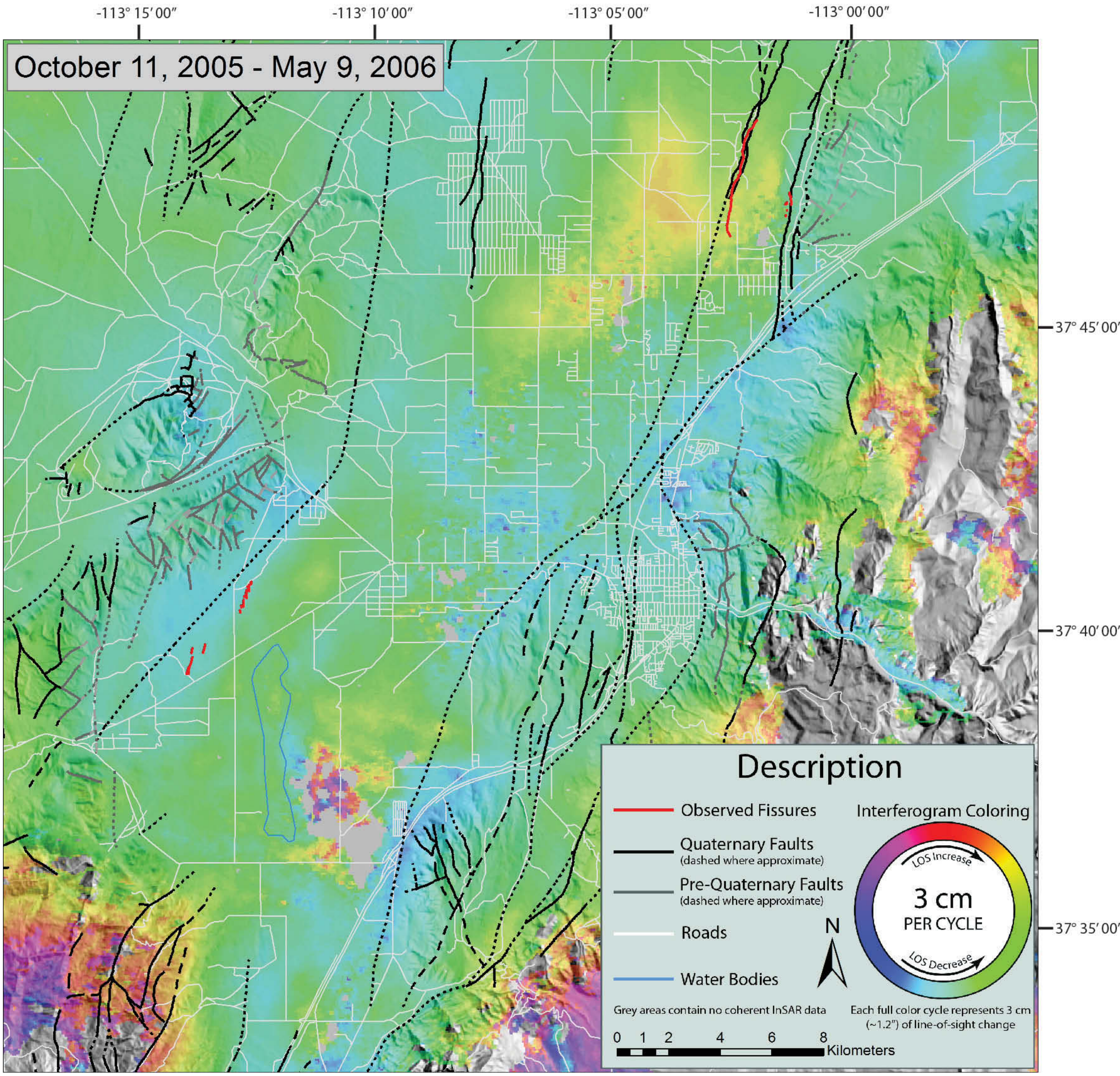

Figure 22. *Unwrapped Envisat interferogram covering the time period of October 11, 2005–May 9, 2006. Fault and fissure data from Knudsen and others (2012). All road, DEM, and water-body data downloaded from the USGS National Map (2011).*

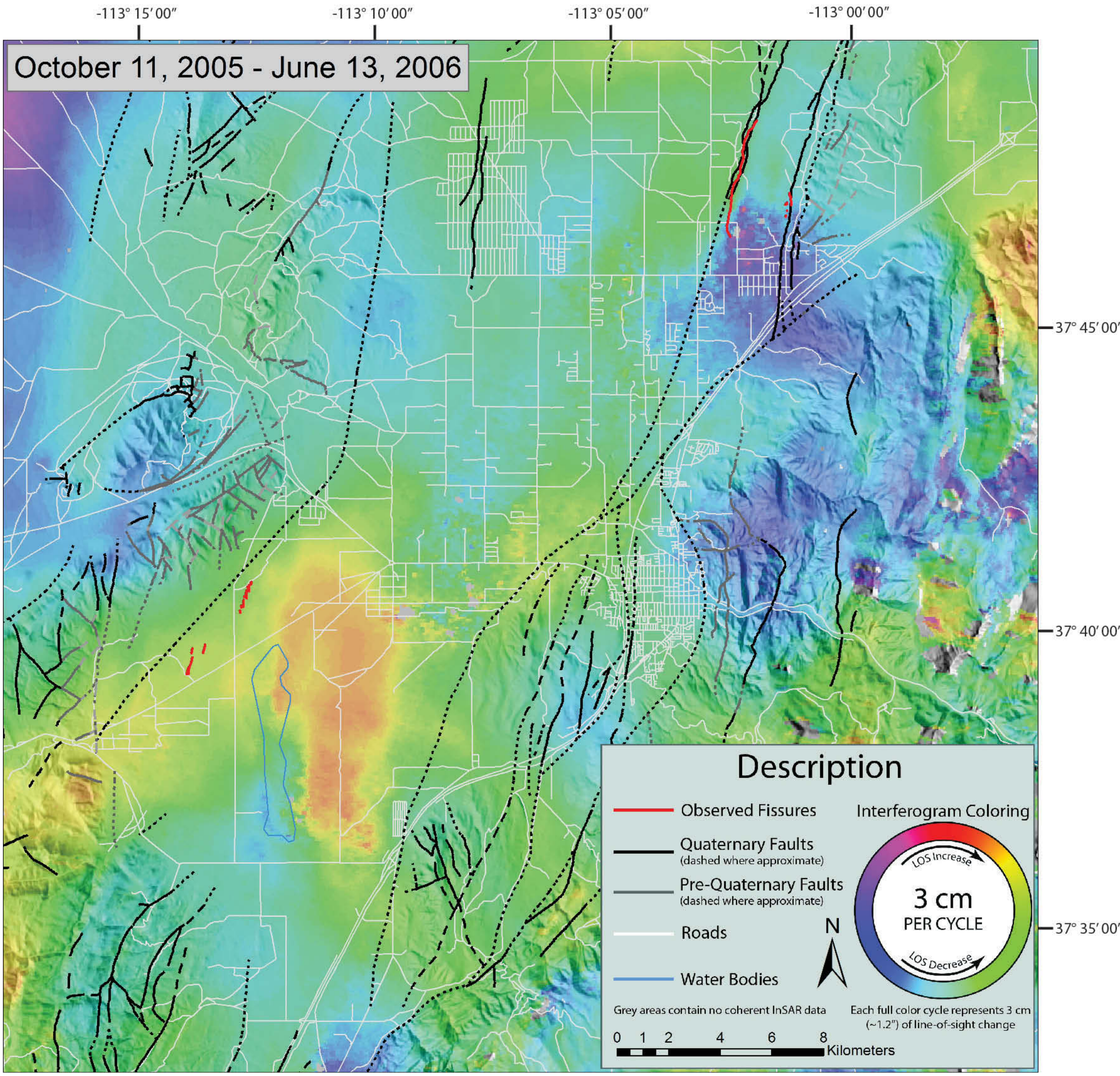

Figure 23. *Unwrapped Envisat interferogram covering the time period of October 11, 2005–June 13, 2006. Fault and fissure data from Knudsen and others (2012). All road, DEM, and water-body data downloaded from the USGS National Map (2011).*

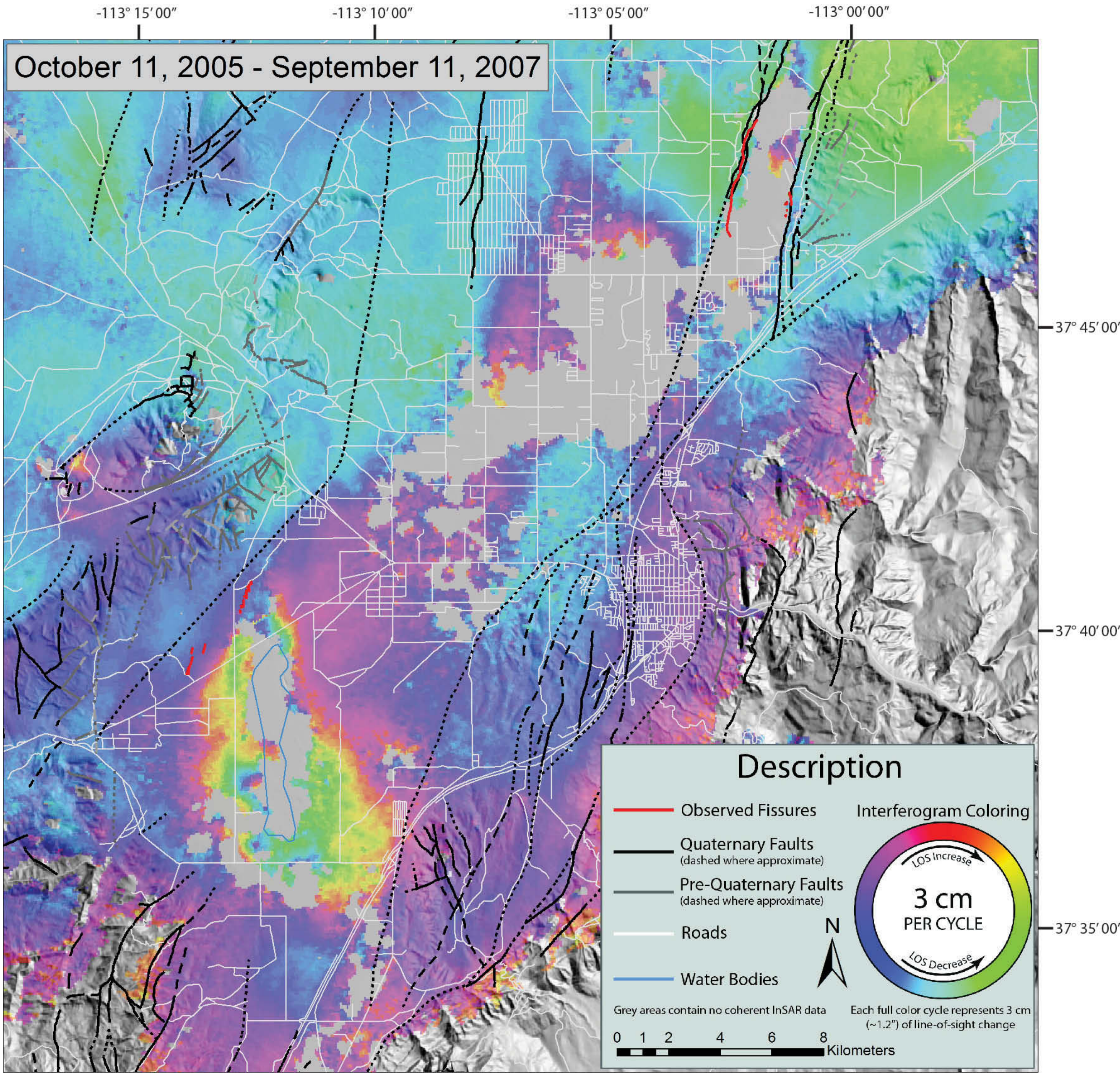

Figure 24. *Unwrapped Envisat interferogram covering the time period of November 15, 2005–September 11, 2007. Fault and fissure data from Knudsen and others (2012). All road, DEM, and water-body data downloaded from the USGS National Map (2011).*

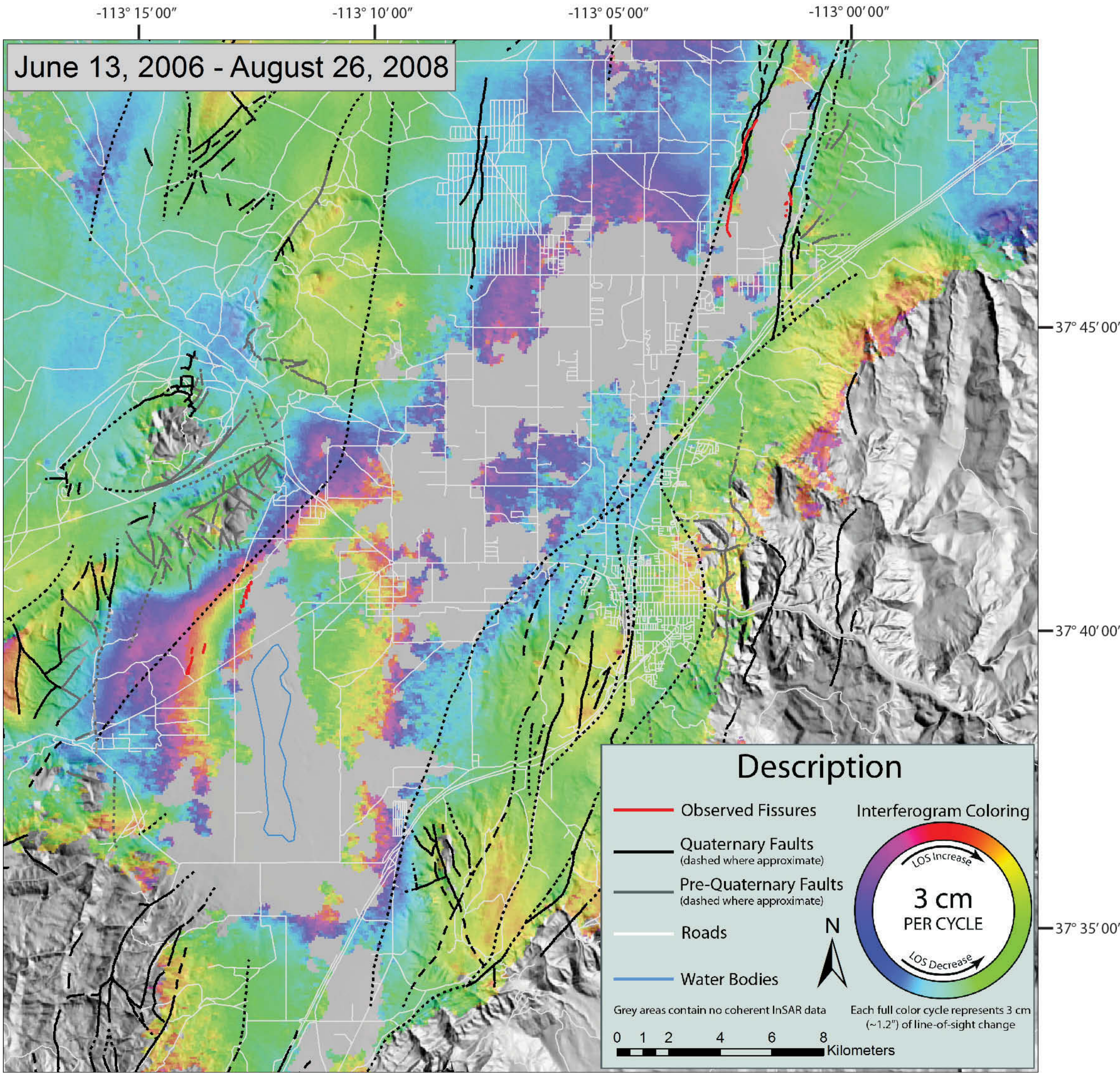

Figure 25. *Unwrapped Envisat interferogram covering the time period of June 13, 2006–August 26, 2008. Fault and fissure data from Knudsen and others (2012). All road, DEM, and water-body data downloaded from the USGS National Map (2011).*

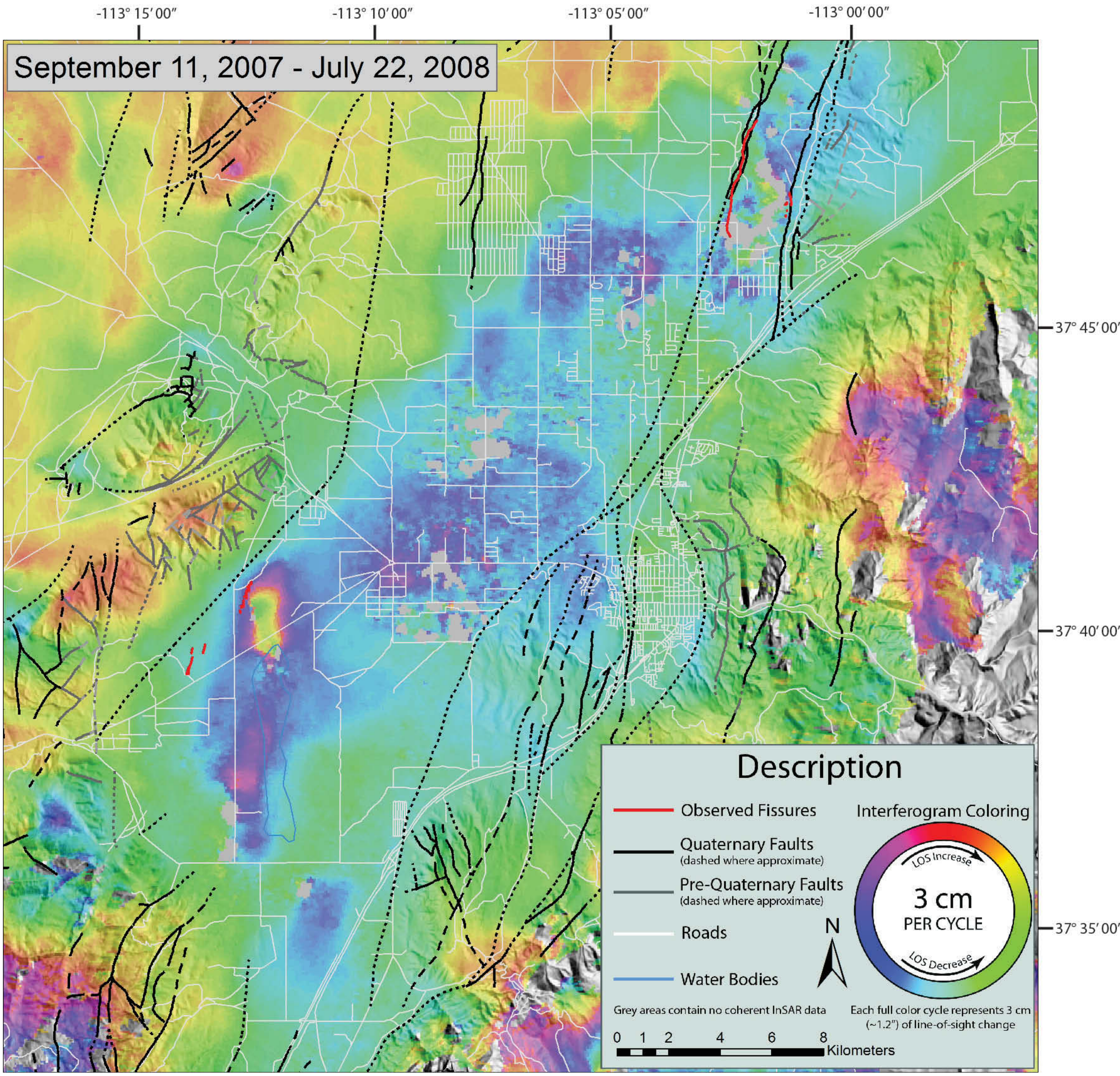

Figure 26. *Unwrapped Envisat interferogram covering the time period of September 11, 2007–July 22, 2008. Fault and fissure data from Knudsen and others (2012). All road, DEM, and water-body data downloaded from the USGS National Map (2011).*

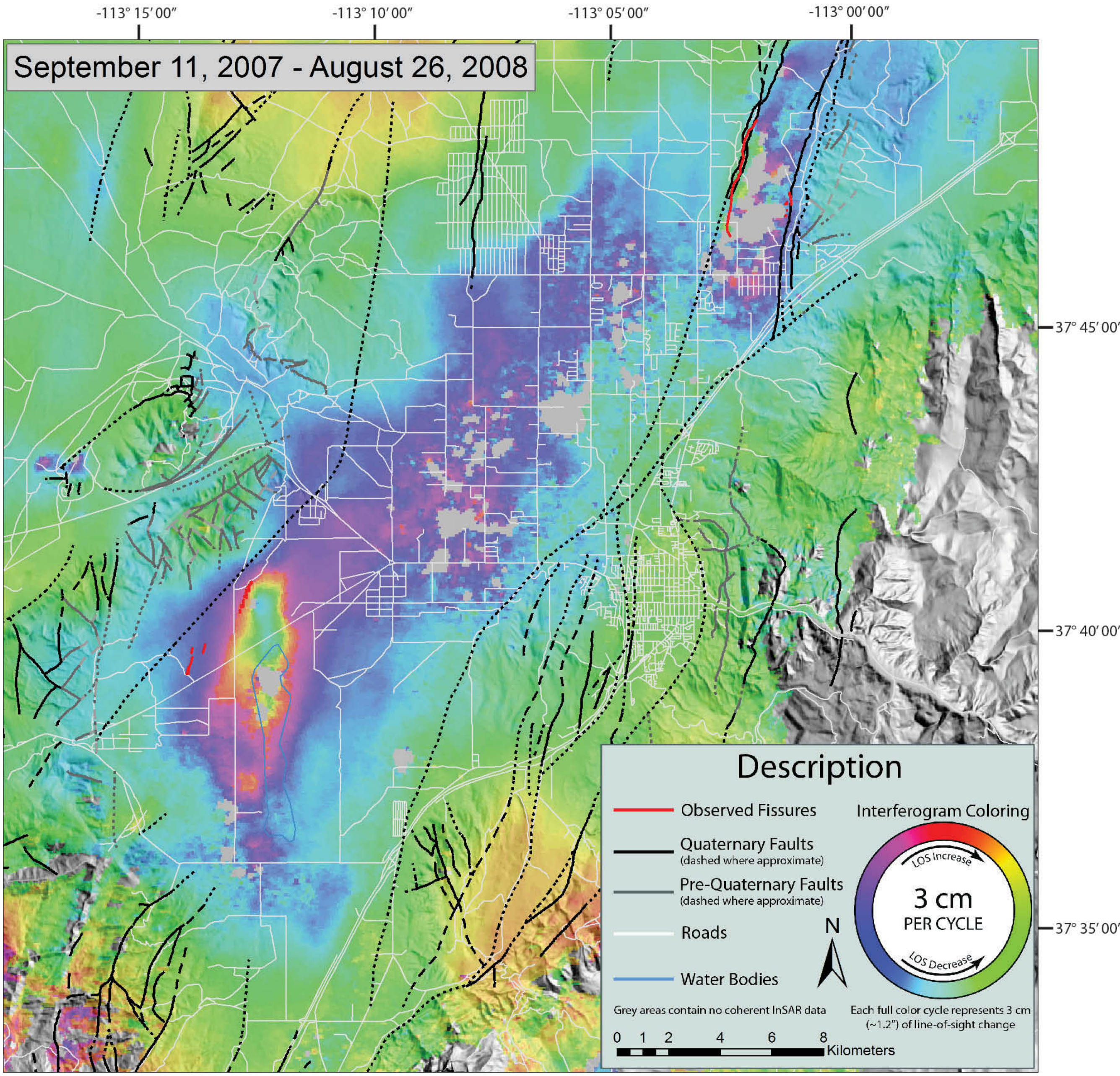

Figure 27. *Unwrapped Envisat interferogram covering the time period of September 11, 2007–August 26, 2008. Fault and fissure data from Knudsen and others (2012). All road, DEM, and water-body data downloaded from the USGS National Map (2011).*

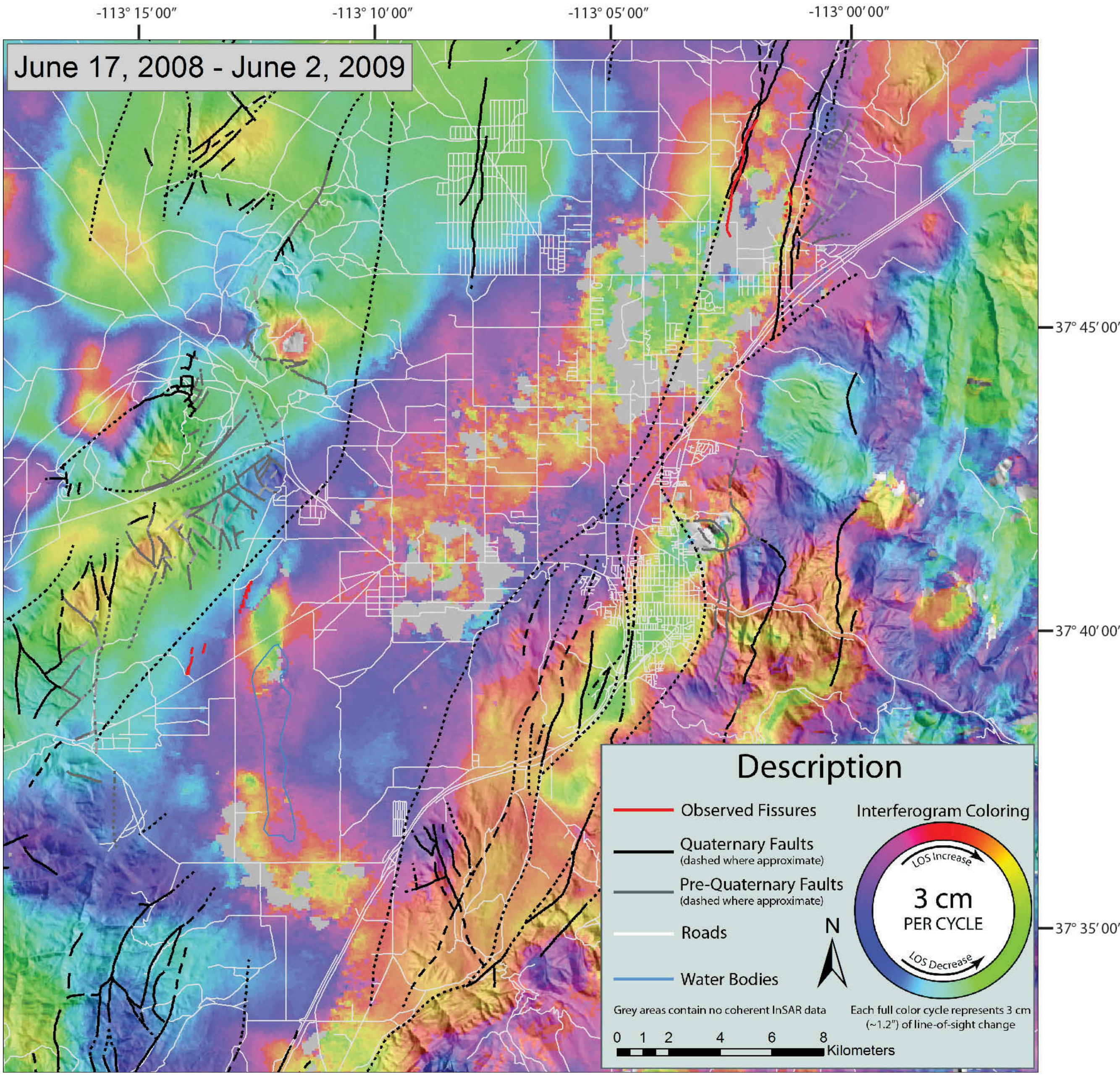

Figure 28. *Unwrapped Envisat interferogram covering the time period of June 17, 2008–June 2, 2009. Fault and fissure data from Knudsen and others (2012). All road, DEM, and water-body data downloaded from the USGS National Map (2011).*

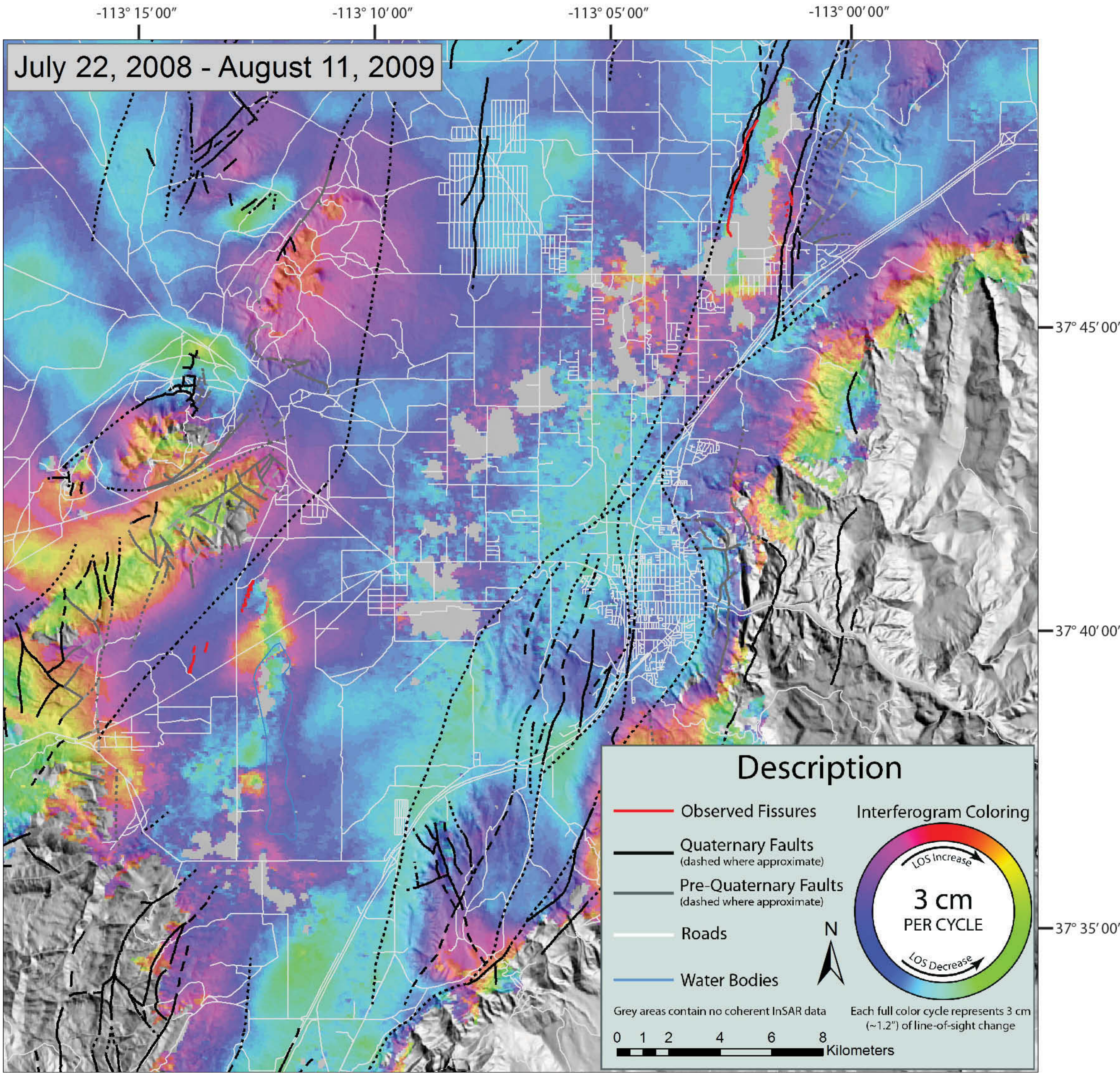

Figure 29. *Unwrapped Envisat interferogram covering the time period of July 22, 2008–August 11, 2009. Fault and fissure data from Knudsen and others (2012). All road, DEM, and water-body data downloaded from the USGS National Map (2011).*

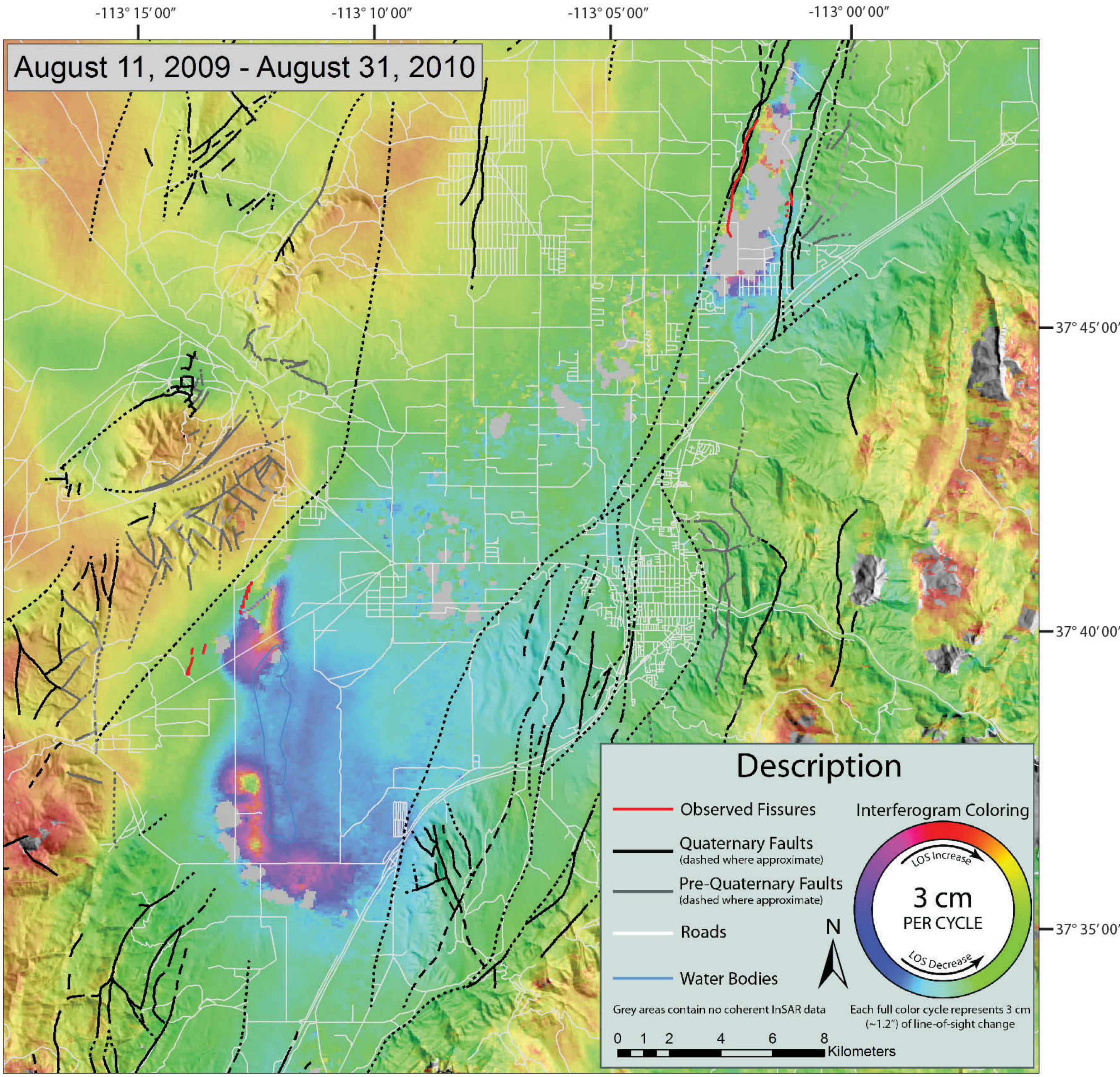

Figure 30. *Unwrapped Envisat interferogram covering the time period of August 11, 2009–August 31, 2010. Fault and fissure data from Knudsen and others (2012). All road, DEM, and water-body data downloaded from the USGS National Map (2011).*

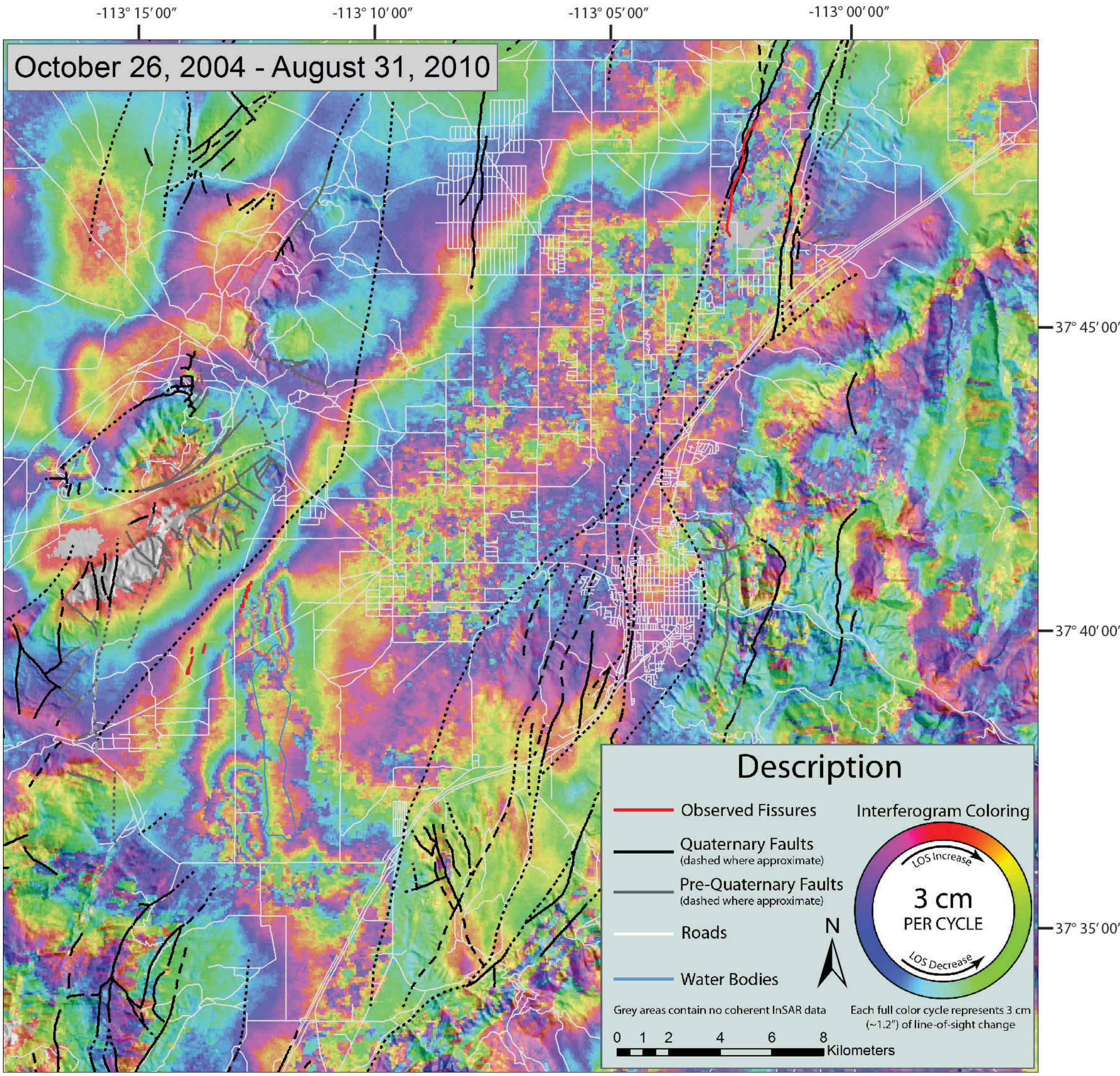

Figure 31. *Semi-cumulative composite, stacked unwrapped Envisat interferogram covering the time period October 26, 2004–August 31, 2010. Note that some pixels were not coherent in all five interferograms used to create the stack. See figure 32 for a masked version of this stack where each pixel with data represents deformation that was coherent in every interferogram used to create the stack. Fault and fissure data from Knudsen and others (2012). All road, DEM, and water-body data downloaded from the USGS National Map (2011).*

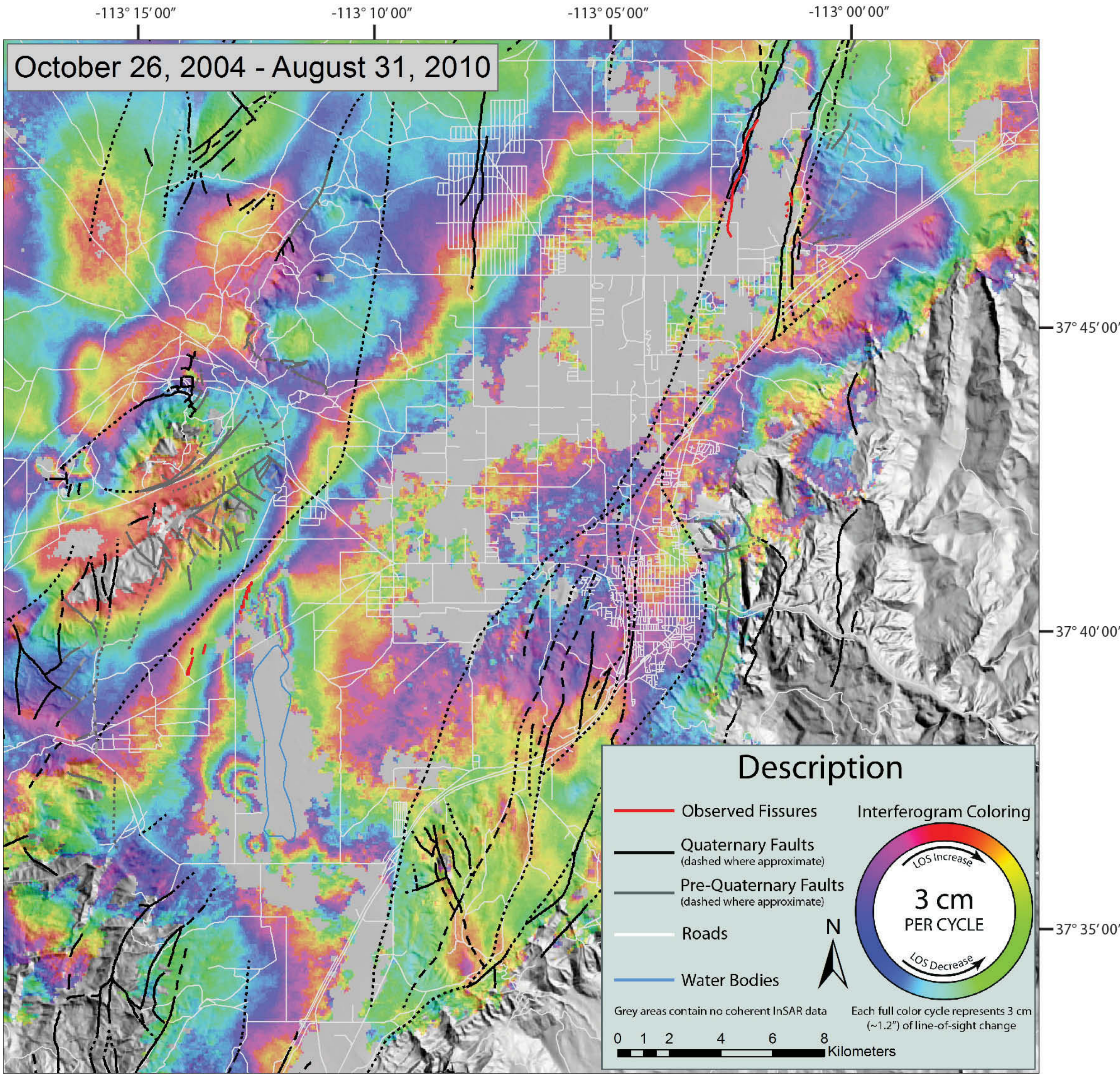

Figure 32. *Semi-cumulative masked, composite, stacked unwrapped Envisat interferogram covering the time period October 26, 2004–August 31, 2010. This stack has been masked such that each pixel with data represents deformation that was coherent in every interferogram used to create the stack. Fault and fissure data from Knudsen and others (2012). All road, DEM, and water-body data downloaded from the USGS National Map (2011).*

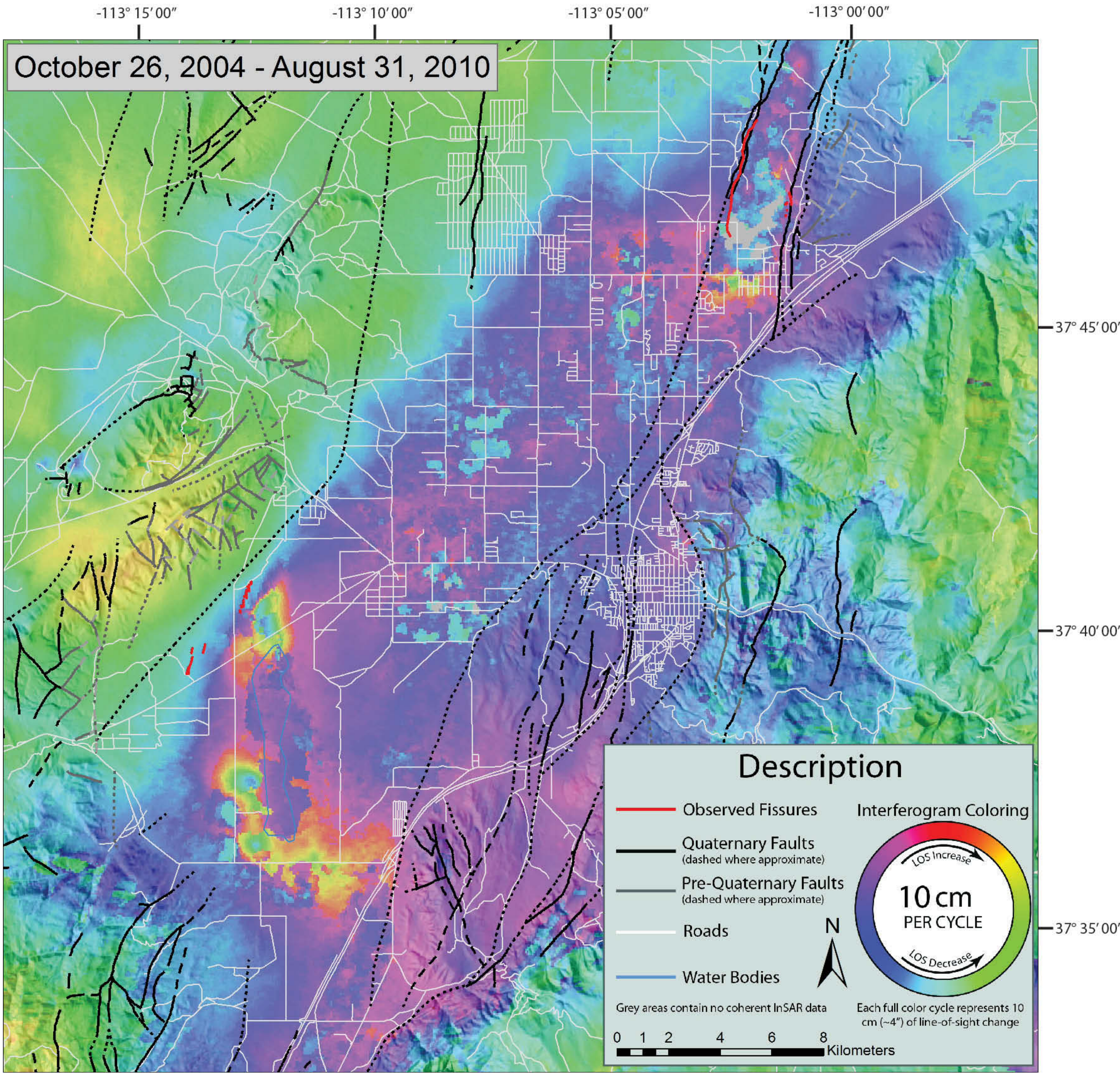

Figure 33. *Semi-cumulative unmasked, composite, stacked unwrapped Envisat interferogram covering the time period of October 26, 2004–August 31, 2010. This stack is identical to the one presented in figure 31, except each color cycle (fringe) represents 10 cm (3.9 in). This was done to present the result in a manner in which topographic and atmospheric noise is subdued while deformation is dominant. Fault and fissure data from Knudsen and others (2012). All road, DEM, and water-body data downloaded from the USGS National Map (2011).*

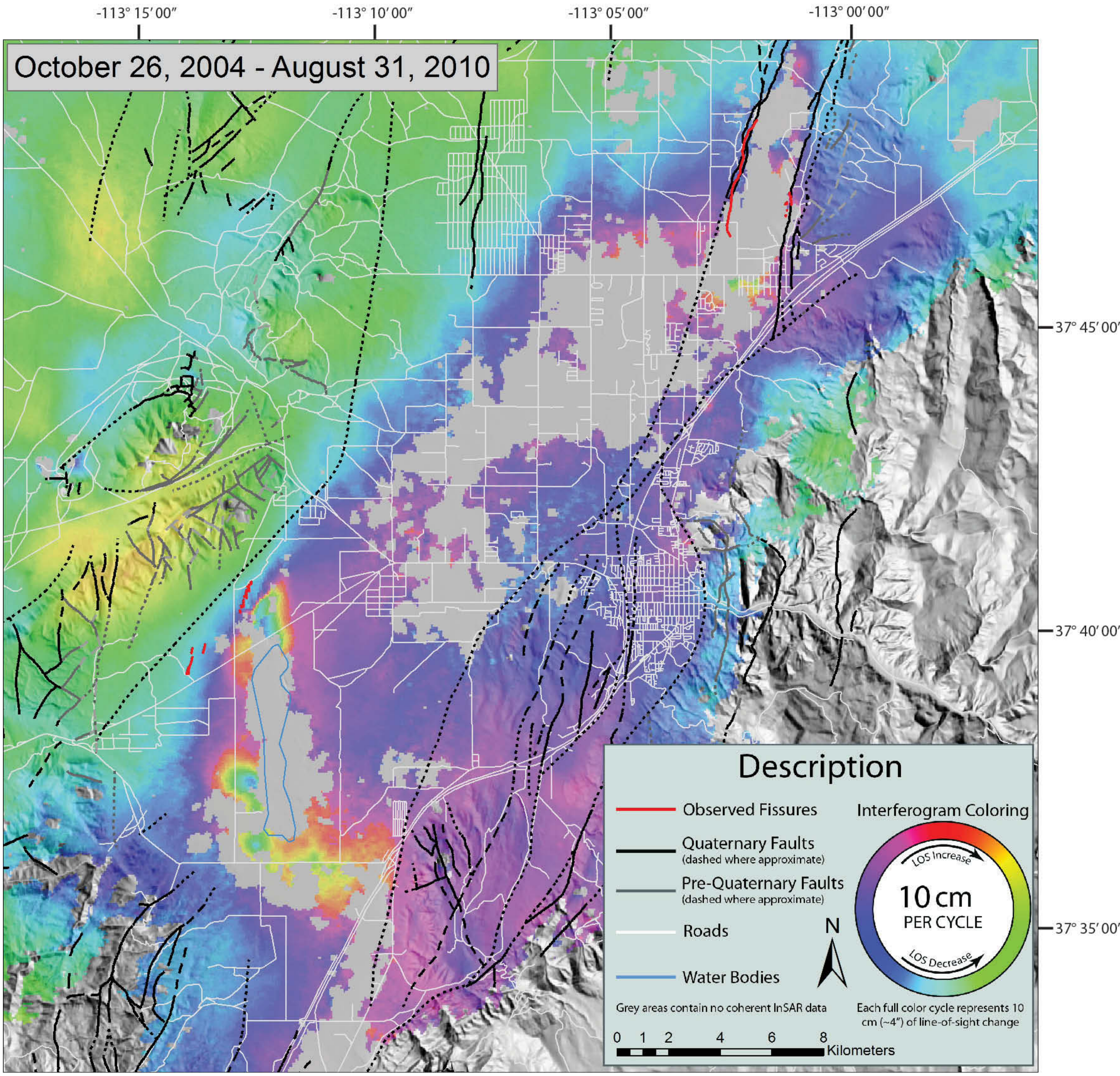

Figure 34. *Semi-cumulative masked, composite, stacked unwrapped Envisat interferogram covering the time period of October 26, 2004–August 31, 2010. This stack is identical to the one presented in figure 32, except each color cycle (fringe) represents 10 cm (3.9 in). This was done to present the result in a manner in which topographic and atmospheric noise is subdued while deformation is dominant. Fault and fissure data from Knudsen and others (2012). All road, DEM, and water-body data downloaded from the USGS National Map (2011)*

ANALYSIS OF INSAR RESULTS

Measurable InSAR deformation signals are visible on nearly all interferograms. The following discussions focus on measured deformation from three general areas: Enoch graben, Quichapa Lake, and central Cedar Valley between these two other sites. It should be noted that the discussion below focuses on the maximum observed values of deformation (i.e., maximum coherent values of deformation) identified in this study. It is possible that larger magnitudes of deformation exist in areas where decorrelation has occurred, and therefore, are unable to be analyzed using this processing methodology. This discussion will focus on the most coherent interferograms created, those that were utilized to create the two stacks.

Enoch Graben

Table 2 shows the maximum values of deformation observed on individual interferograms from within the

Table 2. *Maximum downward deformation observed within the Enoch graben.*

Scene 1 Date (YYMMDD)	Scene 2 Date (YYMMDD)	Maximum Observed Deformation in cm (in)	Maximum Observed Deformation Rate in cm/yr (in/yr)
921114	930612	-0.6 (-0.2)	-1.0 (-0.4)
931030	951023	-1.1 (-0.4)	-0.6 (-0.2)
950919	970715	-1.2 (-0.5)	-0.7 (-0.3)
970715	991102	-0.9 (-0.4)	-0.4 (-0.2)
991102	001017	-2.9 (-1.1)	-3.0 (-1.2)
041026	051115	-1.4 (-0.6)	-1.3 (-0.5)
051115	070911	-1.6 (-0.6)	-0.9 (-0.4)
070911	080722	-2.0 (-0.8)	-2.3 (-0.9)
080617	090602	-1.3 (-0.5)	-1.4 (-0.6)
090811	100831	-1.7 (-0.7)	-1.6 (-0.6)

Table 3. *Maximum downward deformation observed in the vicinity of Quichapa Lake.*

Scene 1 Date (YYMMDD)	Scene 2 Date (YYMMDD)	Maximum Observed Deformation in cm (in)	Maximum Observed Deformation Rate in cm/yr (in/yr)
921114	930612	-0.1 (-0.04)	-0.2 (-0.1)
931030	951023	-1.0 (-0.4)	-0.5 (-0.2)
950919	970715	-1.3 (-0.5)	-0.7 (-0.3)
970715	991102	-1.2 (-0.5)	-0.5 (-0.2)
991102	001017	-1.9 (-0.7)	-2.0 (-0.8)
041026	051115	-2.0 (-0.8)	-1.9 (-0.7)
051115	070911	-4.5 (-1.8)	-2.5 (1.0)
070911	080722	-3.3 (-1.3)	-3.8 (-1.5)
080617	090602	-2.2 (-0.9)	-2.3 (-0.9)
090811	100831	-3.5 (-1.4)	-3.3 (-1.3)

Enoch graben. Deformation rates ranged from -0.4 cm to -3.0 cm (-0.2 in to -1.2 in) per year (note that each maximum may not be occurring at the same location). The range in observed rates may be a result of inconsistent deformation rates resulting from variations in groundwater withdrawal, precipitation, etc., or it may also be a result of inconsistency in interferogram coherence (i.e., in the cases of interferograms with better coherence, maximum deformation values have been recorded more successfully). Unfortunately, due to inconsistent decorrelation in the individual interferograms used to create the stacks, an accurate estimate of total deformation that occurred near the Enoch graben during the two time periods studied is not possible. The maximum cumulative deformation recorded in the two stacks is -2.9 cm and -8.5 cm (-1.1 in and -3.3 in) for the 1992–2000 and 2004–2010 time periods, respectively. As mentioned above, these are the largest observed (coherent) magnitudes and may be underestimates of maximum deformation due to the possibility that larger magnitudes may lie in areas of decorrelation.

Quichapa Lake

Table 3 details the maximum observed deformation magnitudes measured in the vicinity of Quichapa Lake. Maximum values were typically observed either directly north of Quichapa Lake in the vicinity of the observed fissuring, or in the vicinity of the southern half of the lake. Maximum deformation rates observed in individual interferograms varied from -0.2 cm (-0.1 in) per year to -3.8 cm (-1.5 in) per year. Fortunately, correlation was generally good in the vicinity of Quichapa Lake, and a maximum deformation magnitude can be estimated from the stacked interferograms. The maximum observed values of cumulative downward deformation are -5.1 cm (-2.0 in) and -11.9 cm (-4.7 in) during the 1992–2000 and 2004–2010 time periods, respectively. Both of these maximums occurred in the vicinity (just southeast) of the observed fissures north of Quichapa Lake.

Cedar Valley

Table 4 details the maximum observed deformation recorded in central Cedar Valley between the two previous areas. Maximum values were typically observed about 5–10 km (3–6 mi) north to northwest of downtown Cedar City. However, due to the nature of the surface conditions in this area (vegetation, surface disturbance, etc.), decorrelation is present in many of the interferograms so the data in table 4 are the largest observed (coherent) magnitudes and may not represent the largest magnitudes of deformation that could be masked by decorrelation. Observed maximum individual deformation rates ranged from -0.1 cm (-0.04 in) to -3.1 cm (-1.2 in) per year. Unfortunately, as with the area around the Enoch graben, there is significant decorrelation in central Cedar Valley. The maximum observed values of cumulative downward deformation are -3.7 cm (-1.5 in) and -6.1 cm (-2.4 in) for the time periods of 1992–2000 and 2004–2010, respectively.

Deformation Rates

Figures 35–37 are plots of deformation rates calculated from the data in tables 2–4. The horizontal bars next to each point represent the time span over which that deformation rate was calculated, with the point being the center of that time period. Note the general increase in deformation rate throughout the study period.

Table 4. *Maximum downward deformation observed in central Cedar Valley.*

Scene 1 date (YYMMDD)	Scene 2 Date (YYMMDD)	Maximum deformation observed (cm)	Maximum observed deformation rate (cm/yr)
921114	930612	-1.0 (-0.4)	-1.7 (-0.7)
931030	951023	-1.2 (-0.5)	-0.6 (-0.2)
950919	970715	-1.2 (-0.5)	-0.7 (-0.3)
970715	991102	-0.2 (-0.1)	-0.1 (-0.04)
991102	001017	-1.4 (-0.6)	-1.5 (-0.6)
041026	051115	-1.2 (-0.5)	-1.1 (-0.4)
051115	070911	-2.7 (-1.1)	-1.5 (-0.6)
070911	080722	-2.7 (-1.1)	-3.1 (-1.2)
080617	090602	-3.0 (-1.2)	-3.1 (-1.2)
090811	100831	-0.7 (-0.3)	-0.7 (-0.3)

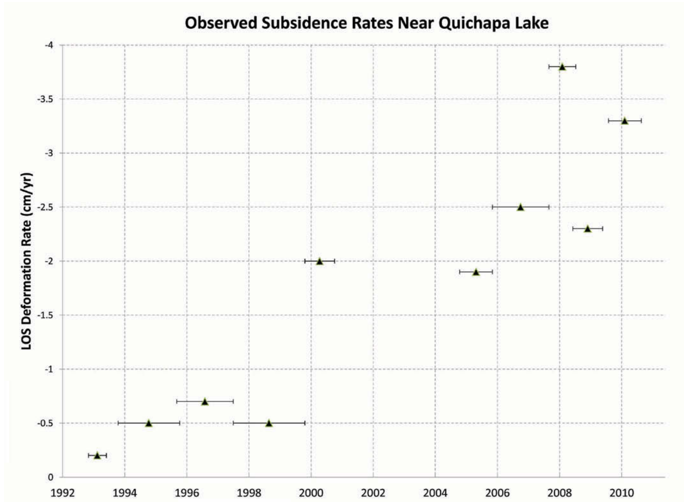

Figure 36. *Plot of maximum observed LOS deformation rate vs. time near Quichapa Lake. Negative values represent elevation decrease along the satellite line of sight (inferred subsidence). Horizontal bars represent the time period covered by the interferograms used to estimate the rates shown.*

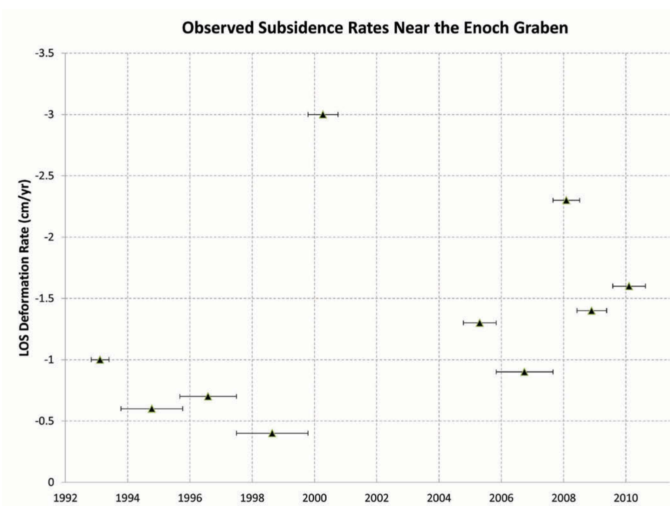

Figure 35. *Plot of maximum observed LOS deformation rate vs. time near the Enoch graben. Negative values represent elevation decrease along the satellite line of sight (inferred subsidence). Horizontal bars represent the time period covered by the interferograms used to estimate the rates shown.*

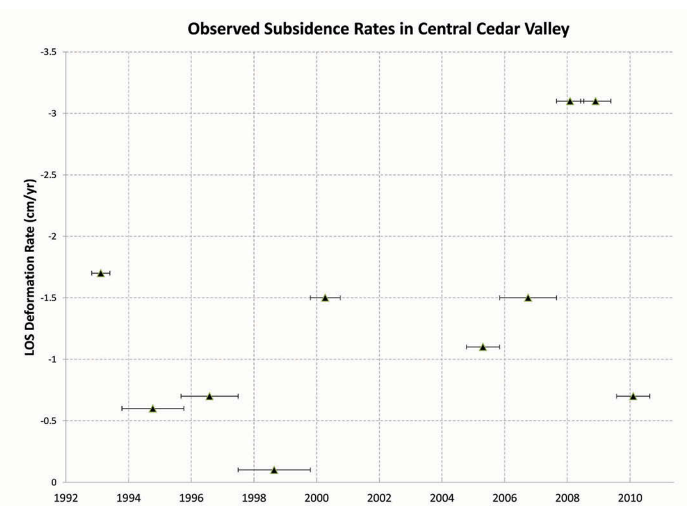

Figure 37. *Plot of maximum observed LOS deformation rate vs. time in central Cedar Valley. Negative values represent elevation decrease along the satellite line of sight (inferred subsidence). Horizontal bars represent the time period covered by the interferograms used to estimate the rates shown.*

Stacked Interferograms and Deformation Contours

In addition to the evaluation of maximum deformation magnitudes and rates presented above, cumulative deformation (subsidence) contours were generated in the vicinity of the areas of interest on two stacked interferograms. The stacked interferograms covering 1992–2000 shown in figures 17–20 were used to create the contours shown in figure 38. However, due to excess noise (likely atmospheric) present in the interferogram covering October 26, 2004–November 15, 2005, a second stack omitting that noisy interferogram was created (figures 39 and 40), such that contour lines could be estimated more accurately. Thus, the contour lines delineated in figure 41 represent deformation recorded during the time period of November 15, 2005–August 31, 2010. When evaluating the contours shown in figures 40 and 41, dashed contours represent areas of lower confidence, and it is important to keep in mind that even the areas delineated with solid contours represent some level of interpretation. Still, these figures represent the best estimation of deformation that is suggested by the most noise-free stacked interferograms.

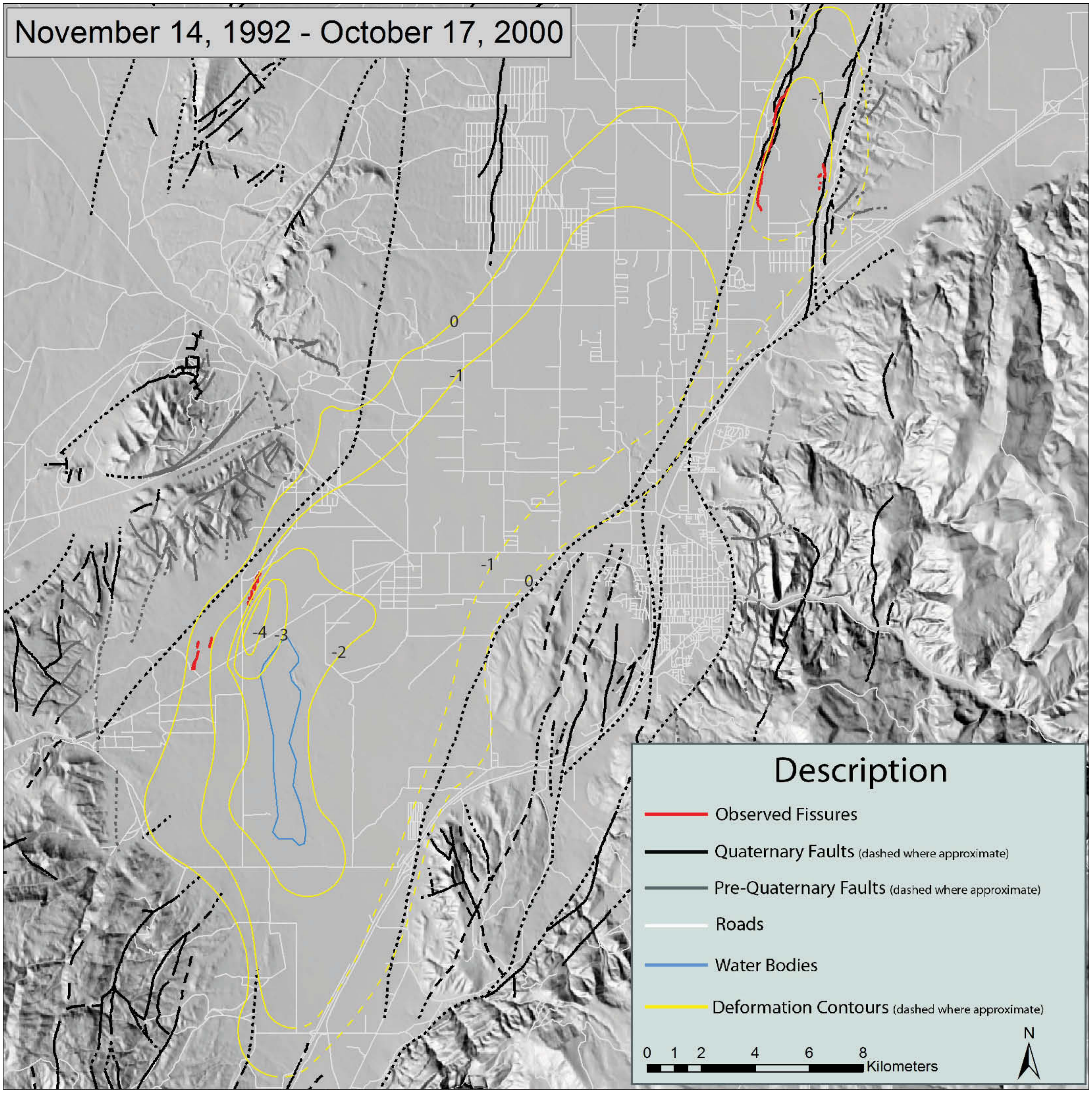

Figure 38. *Contours delineating LOS change (negative values represent a decrease in elevation/subsidence along the satellite line of sight) from November 14, 1992–October 17, 2000, derived from the data displayed in figures 17–20. Contour lines are dashed where estimated or inferred. The approximate total area delineated by the zero contour is 256 km^2 (100 mi^2). Contour interval is 1 cm (0.4 in). Fault and fissure data from Knudsen and others (2012). All road, DEM, and water-body data downloaded from the USGS National Map (2010).*

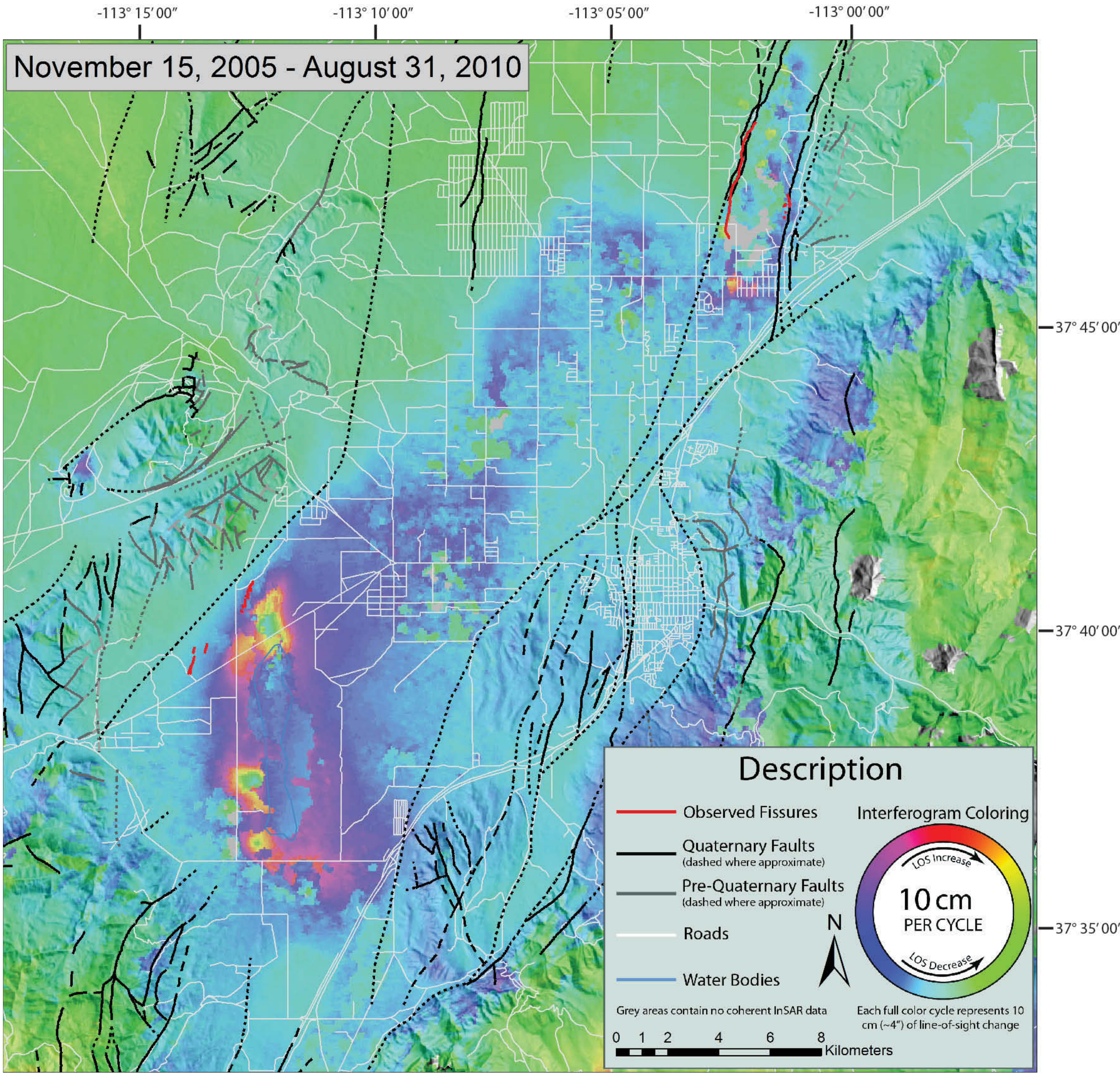

Figure 39. *Semi-cumulative unmasked, composite, stacked unwrapped Envisat interferogram covering the time period of November 15, 2005–August 31, 2010. This stack is the same as the one shown in figure 33, except the interferogram covering October 26, 2004–November 15, 2005, was omitted from the stack in order to reduce noise. Fault and fissure data from Knudsen and others (2012). All road, DEM, and water-body data downloaded from the USGS National Map (2010).*

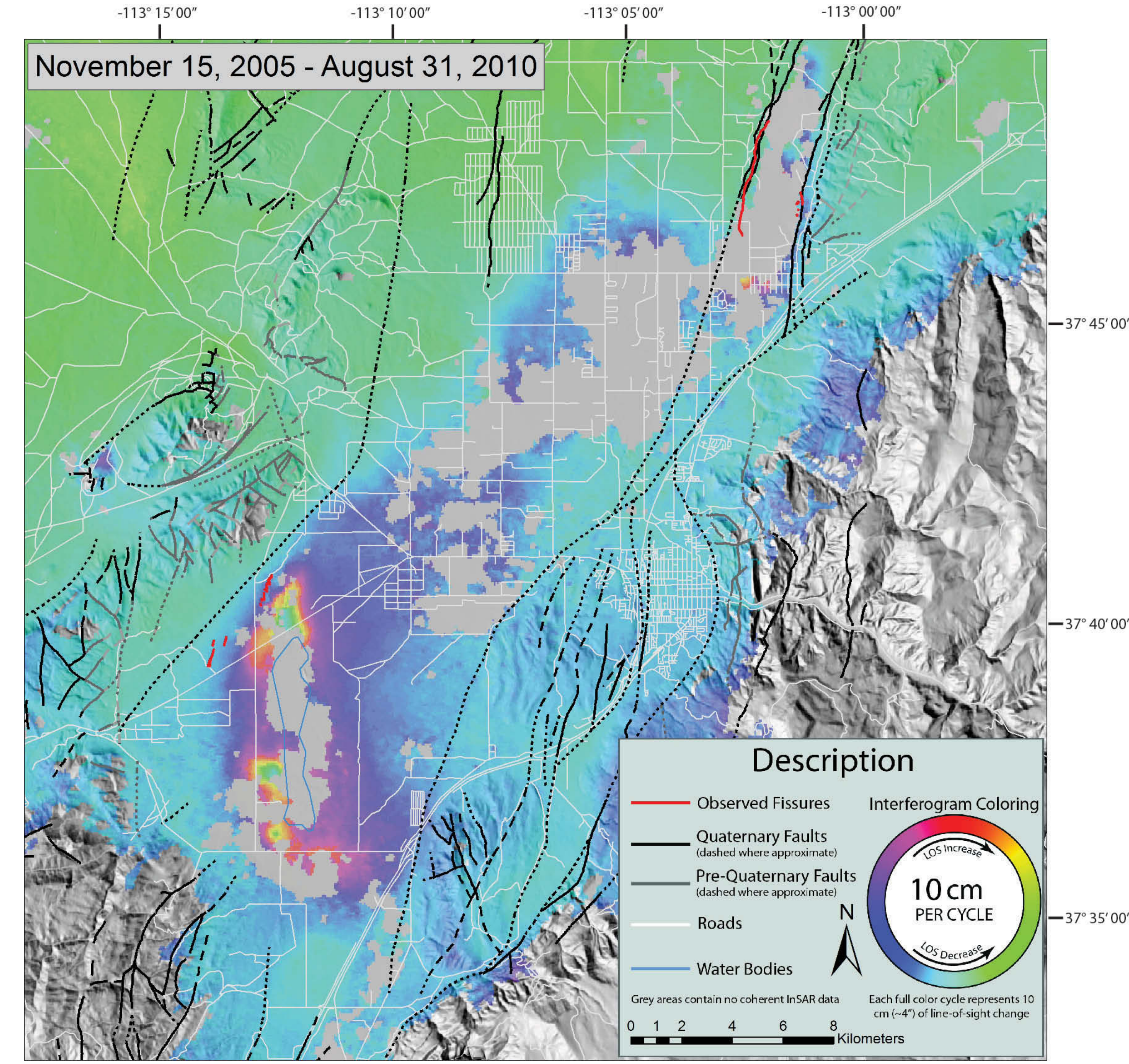

Figure 40. *Semi-cumulative masked, composite, stacked unwrapped Envisat interferogram covering the time period of November 15, 2005–August 31, 2010. This stack is the same as the one shown in figure 34, except the interferogram covering October 26, 2004–November 15, 2005, was omitted from the stack in order to reduce noise. Fault and fissure data from Knudsen and others (2012). All road, DEM, and water-body data downloaded from the USGS National Map (2010).*

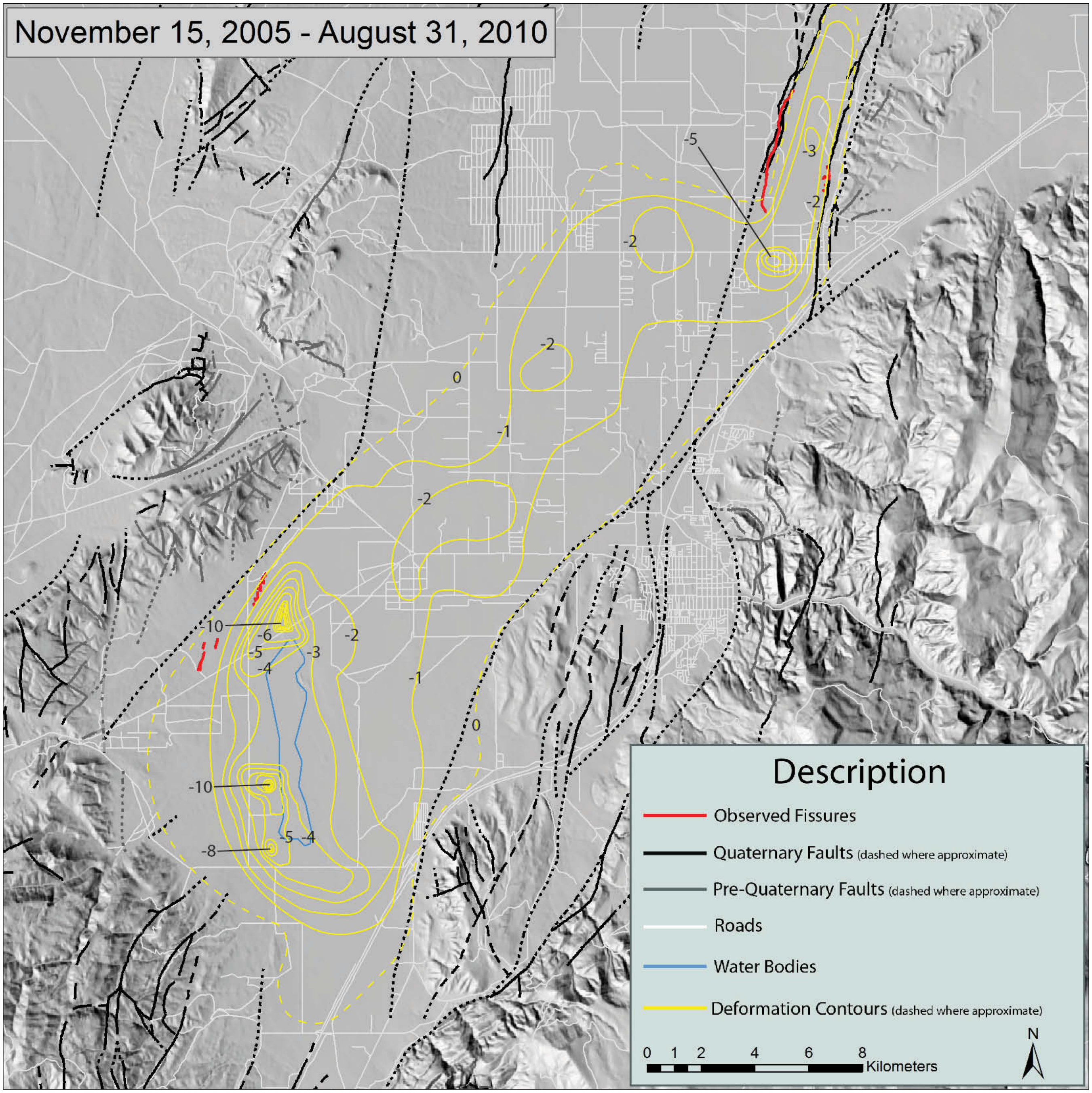

Figure 41. *Contours delineating LOS change (negative values represent a decrease in elevation/subsidence along the satellite line of sight) from November 15, 2005–August 31, 2010, derived from the data displayed in figures 39 and 40. Contour lines are dashed where estimated or inferred. The approximate total area delineated by the zero (dashed) contour is 256 km*^{2} *(100 mi*^{2}*). Due to overprinting in areas of dense contouring, only the maximum value of deformation is labeled in these areas. Contour interval is 1 cm (0.4 in). Fault and fissure data from Knudsen and others (2012). All road, DEM, and water-body data downloaded from the USGS National Map (2010) .*

CONCLUSIONS

The spatial distribution of deformation in Cedar Valley correlates very well with both the location of observed fissuring as well as the location of both municipal and private groundwater production wells as shown in figure 2. Therefore, the fissuring observed near Quichapa Lake as well as within the Enoch graben is very likely a direct result of groundwater pumping in these areas. The total area affected by the deformation is approximately 256 km^2 (100 mi^2). Furthermore, it appears that faults may be controlling the spatial distribution of deformation within the Enoch graben, and possibly along the southeastern boundary of deformation as delineated in the contour maps presented above.

As shown in figures 35–37, the rate of deformation (subsidence) appears to be generally increasing with time at all three areas of interest. However, some uncertainty exists regarding the accuracy of the maximum subsidence magnitudes and associated rates due to decorrelated areas that may hide areas of larger subsidence magnitudes.

REFERENCES

Amelung, F., Galloway, D.L., Bell, J.W., Zebker, H.A., and Laczniak, R.J., 1999, Sensing the ups and downs of Las Vegas—InSAR reveals structural control of land subsidence and aquifer-system deformation: Geology, v. 27, no. 6, p. 483–486.

Buckley, S.M., 2000, Radar interferometry measurement of urban land subsidence: University of Texas at Austin, Ph. D. dissertation, 229 p.

Knudsen, T., Inkenbrandt, P., Lund, W., and Lowe, M., 2012, Investigation of land subsidence and earth fissures in Cedar Valley, Iron County, Utah, for the Central Iron County Water Conservancy District: Utah Geological Survey unpublished contract deliverable, 111 p.

USGS National Map, 2011, United States Geological Survey, accessed November 10, 2011, http://nationalmap.gov/.